

Large-eddy simulations of turbulent flows in arrays of helical- and straight-bladed vertical-axis wind turbines

Cite as: J. Renewable Sustainable Energy **15**, 063309 (2023); doi: 10.1063/5.0172007

Submitted: 12 August 2023 · Accepted: 21 November 2023 ·

Published Online: 13 December 2023








View Online



Export Citation



CrossMark

Masoumeh Charaati,¹  Nathaniel J. Wei,²  John O. Dabiri,^{2,3}  Luis A. Martínez-Tossas,⁴  and Di Yang^{1,a)} 

AFFILIATIONS

¹Department of Mechanical Engineering, University of Houston, Houston, Texas 77204, USA

²Graduate Aeronautical Laboratories, California Institute of Technology, Pasadena, California 91125, USA

³Department of Mechanical and Civil Engineering, California Institute of Technology, Pasadena, California 91125, USA

⁴National Renewable Energy Laboratory, Golden, Colorado 80401, USA

^{a)} Author to whom correspondence should be addressed: diyang@uh.edu

ABSTRACT

Effects of helical-shaped blades on the flow characteristics and power production of finite-length wind farms composed of vertical-axis wind turbines (VAWTs) are studied numerically using large-eddy simulation (LES). Two helical-bladed VAWTs (with opposite blade twist angles) are studied against one straight-bladed VAWT in different array configurations with coarse, intermediate, and tight spacings. Statistical analysis of the LES data shows that the helical-bladed VAWTs can improve the mean power production in the fully developed region of the array by about 4.94%–7.33% compared with the corresponding straight-bladed VAWT cases. The helical-bladed VAWTs also cover the azimuth angle more smoothly during the rotation, resulting in about 47.6%–60.1% reduction in the temporal fluctuation of the VAWT power output. Using the helical-bladed VAWTs also reduces the fatigue load on the structure by significantly reducing the spanwise bending moment (relative to the bottom base), which may improve the longevity of the VAWT system to reduce the long-term maintenance cost.

Published under an exclusive license by AIP Publishing. <https://doi.org/10.1063/5.0172007>

I. INTRODUCTION

In recent years, wind energy has gained considerable growth in market share to help meet the continuously growing energy consumption.^{1,2} Two main types of devices are used to harvest wind energy, namely, the horizontal-axis wind turbine (HAWT) and the vertical-axis wind turbine (VAWT), which are categorized primarily based on the orientation of the turbine rotor axis.^{3,4} Commercially, large-size HAWTs (i.e., exceeding 100 m in rotor diameter) have been widely used in existing and planned onshore and offshore wind farms due to their high rated power output and efficiency.^{4,5} Although VAWTs are less utilized than HAWTs at the current stage, they have gained growing interest in recent years. Compared with HAWTs, VAWTs are much less sensitive to wind direction and do not require yaw control.⁶ VAWTs may achieve potentially faster wake recovery.⁷ VAWTs usually operate at lower tip-speed ratios (TSRs) than HAWTs,^{8,9} which may lead to less acoustic pollution. VAWTs also tend to have smaller footprints than HAWTs and, thus, may be more feasible if land area is limited. All the above-mentioned features make VAWTs potentially suitable to serve as valuable complements to HAWTs (e.g., to be

deployed at places where large HAWTs are not feasible) to help meet the increasing demand for clean and renewable energy.

Unlike HAWTs that have highly converged fundamental design of the rotor,^{3,4} currently there exist various designs for VAWTs, which are differed primarily by the blade geometries.^{8,10} Among different VAWT types, the straight-bladed Darrieus-type VAWTs (hereinafter referred to as the straight-bladed VAWTs) have gained popularity due to the simplicity for designing and manufacturing and, thus, have been also studied more in research.^{9,11–19} The helical-bladed VAWTs, which can be regarded as a variant version of the straight-bladed VAWTs with twisted blades, have also drawn increasing attention in recent years.^{19–24} Recent experimental¹⁹ and numerical²⁴ studies have shown that changing the blade geometry from straight to helical can induce additional mean vertical motion in the VAWT wake flow, which can cause noticeable impact to the turbulence statistics and kinetic energy entrainment that affect the wake speed recovery. However, these effects induced by the helical blades were studied based on the wake characterization of a single VAWT. For practical applications (such as commercial wind farms), a number of VAWTs are typically installed

closely in an array for wind energy harvesting. Therefore, it is desired to further investigate the potential effects of helical-bladed VAWTs in wind farm environments.

To date, previous studies on wind farm flows have focused heavily on HAWT-based farms^{25–34} due to the commercial popularity and success of HAWTs. In contrast, there are only a limited number of studies for VAWT-based farms.^{7,14,17,35–37} Moreover, previous numerical studies on VAWT array flows^{17,37} considered arrays of “infinite” streamwise length by using periodic condition on the streamwise boundaries. Despite the valuable insights gained from these idealized infinite-length VAWT farm studies for understanding the fundamental flow characteristics, they cannot capture the streamwise development of the flow through the finite-size array. On the other hand, field experiments of finite-size VAWT arrays can characterize flow phenomena based on realistic conditions but face challenges for measuring the array-scale flow field information. While measurement techniques such as three-dimensional (3D) particle-tracking velocimetry (PTV)^{18,19} can obtain detailed flow field information within a limited measurement window, it is challenging to extend the measurement to the array scale. To obtain field data at array scale, Kinzel *et al.*⁷ used a measurement system with seven three-component ultrasonic anemometers (Campbell Scientific CSAT3) mounted on a 10 m meteorological tower (Aluma-Towers Inc.) to measure the flow velocity at 11 different positions along the center of a VAWT array. Based on these measurement data, the two-dimensional (2D) contours of the mean velocity, kinetic energy flux, and turbulent intensity were mapped. However, due to the high cost of building multiple sensor towers, the measurements at the 11 positions were not conducted simultaneously,⁷ requiring careful calibration and coordination of the measurements and making it challenging to further improve the spatial resolution of the mapped contours.

Aiming at obtaining the full-field flow information of the entire VAWT array, in this study the large-eddy simulation (LES) model in Gharaati *et al.*²⁴ is further extended to simulate the interactions between boundary-layer turbulence and large VAWT arrays. Similar to Gharaati *et al.*,²⁴ three VAWTs with identical key parameters but different blade geometries are considered: one with straight blades and the other two with helical blades twisted in opposite directions. The three VAWTs are configured based on the commercial three-blade helical VAWT used in the experiments of Wei *et al.*,¹⁹ which has a rotor equator height of 8.2 m, a rotor diameter of 1.8 m, a blade vertical length of 3.2 m, and a blade twist rate of 39.69°/m. For the VAWT array configuration, three different streamwise/spanwise spacings are considered, covering coarse (56 VAWTs), intermediate (176 VAWTs), and tight (208 VAWTs) layouts. In each case, individual VAWTs in the array rotate independently based on the local inflow condition at a fixed TSR of 1.19 (determined based on the field measurement¹⁹) and are modeled using the actuator line method (ALM) that has been widely used in prior LES modeling of VAWTs and HAWTs.^{9,38–49} The VAWT arrays have finite streamwise length. The inflow of the VAWT array is obtained from a precursor LES model of fully developed boundary layer turbulence, which is coupled with the LES model of the VAWT array flows through a concurrent precursor simulation method.^{29,31} In total, nine computationally expensive LES cases are performed to obtain the full 3D flow data of the VAWT arrays. Based on the LES data, systematic statistical analyses are performed to characterize the effects of VAWT helical

geometry on the turbulent flow statistics, VAWT power rate, and VAWT tower bending moment.

The remainder of this paper is organized as follows. In Sec. II, the LES-ALM model for simulating the wind farms is elaborated. Section III explains the setup of the LES cases. In Sec. IV, the effects of VAWT blade geometry on the flow characteristics in the turbine array are analyzed based on the LES data. Finally, conclusions are presented in Sec. V.

II. DESCRIPTION OF LARGE-EDDY SIMULATION MODEL

In the present study, the open-source LES model of turbulent flows developed by the Turbulence Research Group at Johns Hopkins University, i.e., the LESGO model,⁵⁰ is adopted and modified to simulate the interaction of boundary-layer turbulence with the array of VAWTs. The flow system in the LES model is formulated based on the 3D Cartesian coordinates $x_i (i = 1, 2, 3) = (x, y, z)$, where x , y , and z are the coordinates for the streamwise, spanwise, and vertical directions, respectively. The corresponding 3D velocity vector is denoted as $u_i (i = 1, 2, 3) = (u, v, w)$, where u , v , and w are the velocity components in the x -, y -, and z -directions, respectively. The wind turbulence is simulated by solving the following filtered Navier–Stokes equations for incompressible flow, which are written in the index notation form as

$$\begin{aligned} \frac{\partial \tilde{u}_i}{\partial x_i} &= 0, \\ \frac{\partial \tilde{u}_i}{\partial t} + \tilde{u}_j \left(\frac{\partial \tilde{u}_i}{\partial x_j} - \frac{\partial \tilde{u}_j}{\partial x_i} \right) &= -\frac{\partial \tilde{p}^*}{\partial x_i} + \nu \frac{\partial^2 \tilde{u}_i}{\partial x_j \partial x_j} - \frac{\partial \tau_{ij}^d}{\partial x_j} + \frac{f_{p,i}}{\rho} \delta_{i1} - \frac{\tilde{f}_{e,i}}{\rho}. \end{aligned} \quad (1)$$

Here, (\dots) denotes the filtering at the LES grid scale Δ ; $\tilde{u}_i = (\tilde{u}, \tilde{v}, \tilde{w})$ is the resolved flow velocity; ρ is the density of air; ν are the kinematic viscosity of air; $\tau_{ij}^{sgs} = \tilde{u}_i \tilde{u}_j - \tilde{u}_i \tilde{u}_j$ is the subgrid-scale (SGS) flow stress tensor; $\tau_{ij}^d = \tau_{ij}^{sgs} - \delta_{ij} \tau_{kk}^{sgs}/3$ is the deviatoric part of τ_{ij}^{sgs} , where τ_{kk}^{sgs} is the trace and δ_{ij} is the Kronecker delta; \tilde{p}^* is the modified pressure; f_p is an imposed pressure gradient force to drive the flow; and $\tilde{f}_{e,i}$ represents the turbine-induced forces to the wind. In particular, the aerodynamic forces induced by the VAWT blades are modeled using ALM,³⁸ and the modeled forces are smoothly distributed onto the LES computational grids using a 3D Gaussian kernel method.^{38,40,41,43} More details of ALM for modeling $\tilde{f}_{e,i}$ are given in Appendix A.

In the LES model, τ_{ij}^d is modeled using the Lilly–Smagorinsky eddy-viscosity type model,^{51,52} i.e., $\tau_{ij}^d = -2\nu_{sgs} \tilde{S}_{ij} = -2(c_s \Delta) |\tilde{S}| \tilde{S}_{ij}$, where $\tilde{S}_{ij} = (\partial \tilde{u}_j / \partial x_i + \partial \tilde{u}_i / \partial x_j) / 2$ is the resolved strain-rate tensor, $|\tilde{S}| = \sqrt{2 \tilde{S}_{ij} \tilde{S}_{ij}}$, $\nu_{sgs} = (c_s \Delta) |\tilde{S}|$ is the SGS eddy viscosity, and c_s is the Smagorinsky model coefficient. In the current LES study, the local and instantaneous value of c_s is determined dynamically during the simulation using the Lagrangian-averaged scale-dependent dynamic (LASD) model.⁵³ In particular, the LASD model employs the core idea of the dynamic Smagorinsky model approach of Germano *et al.*,⁵⁴ i.e., the Germano identity equation that relates the resolved turbulent stress to the SGS stresses at different scales. However, the original dynamic Smagorinsky model⁵⁴ assumes c_s to be scale invariant and evaluates its value by performing horizontal averaging, which can lead to inaccurate results when modeling wall-bounded turbulence with horizontal heterogeneity (e.g., the wind farm flows). The LASD model⁵³ overcomes

these weaknesses by allowing c_s to be scale dependent^{55,56} and evaluating its value by Lagrangian average along fluid trajectories instead of horizontal average.⁵⁷ The LASD model has been successfully applied to model the SGS turbulence effects in turbine wake flows in several prior LES studies.^{24,26,27,29,30,32–34,58}

Equations (1) and (2) are discretized using the Fourier-series-based pseudo-spectral method in the x - and y -directions on collocated grids, and the second-order central difference method in the z -direction on staggered grids. In the basic LES solver, the periodic condition is used at the lateral boundaries in the x - and y -directions. The free-slip rigid-lid condition ($\partial\tilde{u}/\partial z = \partial\tilde{v}/\partial z = 0, \tilde{w} = 0$) is applied at the top boundary, which has been commonly used for modeling atmospheric boundary layer turbulence, canopy flows, and wind farm flows.^{17,26,27,29,30,53,59–62} The local law-of-the-wall condition^{53,59–61} is applied at the bottom boundary, in which the wall surface shear stress components ($\tau_{i3}^{\text{wall}}, i = 1, 2$) are modeled as⁵³

$$\tau_{i3}^{\text{wall}}(x, y, t) = - \left[\frac{\kappa}{\ln(d_2/z_0)} \right]^2 \{ [\hat{u}_1(x, y, d_2, t)]^2 + [\hat{u}_2(x, y, d_2, t)]^2 \}^{1/2} \hat{u}_i(x, y, d_2, t), \quad (3)$$

where $\hat{(\)}$ represents filtering at the scale 2Δ , $d_2 = \Delta z/2$ is the height of the first grid point above the bottom boundary, z_0 is the SGS surface roughness, and $\kappa = 0.4$ is the von Kármán constant.

The simulation is advanced in time using a fractional-step method, which consists of a velocity prediction step and a pressure correction step. Full details of the numerical schemes used in the LESGO model are given in Albertson⁶³ and Albertson and Parlange.⁶⁰

III. SETUP OF SIMULATION CASES

In this study, one straight-bladed VAWT and two helical-bladed VAWTs are considered. Table I lists the key parameters of the VAWTs. Except for the geometry of the blades, all three VAWT types have identical key parameters as summarized here. In particular, each VAWT is composed of three blades (i.e., $N_b = 3$) with a cross-sectional shape of the NACA0018 airfoil (with a chord length of $c = 0.511$ m and a thickness of $t_b = 0.092$ m). The turbine rotor radius (i.e., the radial distance from the central axis to the chord of each blade) is $R = 0.9$ m; the rotor diameter is $D = 2R = 1.8$ m; the rotor vertical height is $H = 3.2$ m; and the VAWT equator height (i.e., the mid-height of the blades) is at $z_{\text{eq}} = 8.2$ m above the ground. The corresponding turbine solidity is $\sigma = N_b c / \pi D \approx 0.271$. In the

TABLE I. Key parameters of VAWTs.

Number of blades (N_b)	3
Rotor radius (R)	0.9 m
Rotor diameter (D)	1.8 m
Rotor vertical height (H)	3.2 m
Rotor equator height (z_{eq})	8.2 m
Blade cross-sectional shape	NACA 0018 airfoil
Blade chord length (c)	0.511 m
Blade thickness (t_b)	0.092 m
Turbine solidity ($\sigma = N_b c / \pi D$)	0.271
Blade twist angle (γ)	$0^\circ, \pm 127^\circ$

simulations, all VAWTs are set to rotate at a fixed TSR of $\lambda = R\Omega/U_{\text{ref}} = 1.19$ chosen based on the field measurement value reported in Wei *et al.*,¹⁹ where Ω is the angular speed of the VAWT rotation and U_{ref} is the local reference velocity based on the average of the instantaneous wind velocity sampled along the centerline at 1D upstream of the corresponding VAWT. Compared with the straight-bladed VAWT, the two helical-bladed VAWTs have the blades twisted in opposite directions with a fixed twist rate of 39.69° per meter height,¹⁹ yielding a total twist angle of 127° over the vertical height of $H = 3.2$ m. Taking the top end of the blade as the reference, if the blade is twisted counterclockwise toward the bottom end, the twist angle γ between the top and bottom edges of the blade is defined to be positive. Conversely, if the blade is twisted clockwise from top to bottom, the twist angle is defined as negative, i.e., $\gamma = -127^\circ$. It should be noted that the $\gamma = -127^\circ$ helical-bladed VAWT considered in this study is analogous to the commercial VAWT studied in the field measurement by Wei *et al.*,¹⁹ but with both blade orientation and direction of rotation of the VAWT mirrored.²⁴ Also, the cross-sectional airfoil profile considered in the current study does not match precisely with that of the commercial VAWT studied in Wei *et al.*¹⁹ The commercial helical-bladed VAWT uses a nonstandard cross-sectional aerodynamic profile, for which the lift and drag coefficients are not available. Here, we choose the NACA0018 airfoil profile for modeling because of the accessibility of its lift and drag coefficients data.⁶⁴ As shown in Gharaati *et al.*,²⁴ the essential effects of the VAWT helical geometry on the wake flow characteristics can still be captured despite the differences in the blade cross-sectional profile.

In this study, we focus on investigating the effects of blade geometry when VAWTs are deployed in array configurations. The VAWT arrays have finite streamwise length and interact with a fully developed neutral turbulent boundary layer inflow. To achieve this in the simulations, the concurrent precursor method developed by Stevens *et al.*²⁹ is employed, which is illustrated in Fig. 1. In particular, all simulation cases are configured with a precursor simulation domain of size $(L_x^p, L_y, L_z) = (144, 144, 20)$ m for modeling the fully developed turbulent boundary layer inflow, and a main simulation domain of size $(L_x, L_y, L_z) = (165.6, 144, 20)$ m $= (92D, 80D, 11.11D)$ for modeling the VAWT array. Additional tests with an increased domain height (see Appendix B) have confirmed that the 20 m domain height chosen for the reported simulations is adequate. The precursor and main simulation domains are adjacent at $x = 0$, i.e., the precursor simulation domain occupies $x \in [-L_x^p, 0]$ and the main simulation domain occupies $x \in [0, L_x]$. Following prior LES studies of finite-length wind farms,^{29,31} the precursor simulation domain utilizes periodic boundary conditions in the x - and y -directions to obtain the fully developed boundary-layer turbulence. The main simulation domain utilizes the inflow–outflow boundary condition in the x -direction and periodic boundary condition in the y -direction. In order to apply the inflow–outflow condition properly in the Fourier-series-based pseudo-spectral LES model, the main simulation domain employs the fringe-zone method.^{65–67} As illustrated in Fig. 1, a fringe zone with a streamwise length of $L_{\text{fr}} = L_x/8 = 11.5D = 20.7$ m is adjacent to the outflow boundary, i.e., at $x \in [x_{\text{fr}}, L_x]$, where $x_{\text{fr}} = L_x - L_{\text{fr}} = 7L_x/8 = 80.5D$. This fringe zone serves as a buffer layer to make the exiting flow near the downstream boundary transition smoothly to the inflow condition imposed by precursor simulation at the upstream boundary, which allows the application of the inflow–outflow condition in the

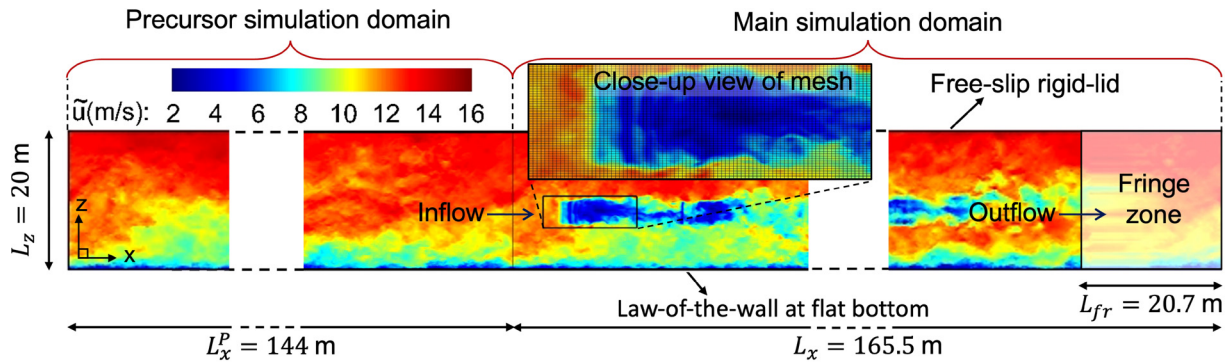


FIG. 1. Illustration of concurrent precursor method and boundary conditions to simulate wind farm. A close-up view of the computational mesh around the first VAWT is also shown. Due to limited space, the middle parts of the precursor and main simulation domains are skipped (as indicated by the dashed lines).

periodic spectral solver.^{24,29,68} In particular, within this fringe zone, the flow velocity vector in the LES solver is imposed as²⁹

$$\tilde{u}_i(x, y, z, t) = \tilde{u}_i(x_{fr}, y, z, t)[1 - \psi(x)] + \tilde{u}_{in,i}(y, z, t)\psi(x) \quad \text{at } x \in [x_{fr}, L_x], \quad (4)$$

where $\psi(x) = 0.5 - 0.5 \cos[\pi(x - x_{fr})/L_{fr}]$ is the fringe function, and $\tilde{u}_{in,i}$ is the inflow velocity for the main simulation extracted in real time from the precursor simulation at $x = 0$. This concurrent precursor simulation method has been successfully applied in several prior LES studies of wind turbine flows.^{24,29,31}

Table II summarizes the key parameters for the VAWT array layouts considered in this study. In each case, VAWTs of the same type are placed in an array consisting of aligned rows (i.e., along the y -direction) and columns (i.e., along the x -direction). Following Calaf *et al.*,²⁶ the turbine spacing parameters in the x - and y -directions are defined as $S_x = \Delta L_x/D$ and $S_y = \Delta L_y/D$, respectively, where ΔL_x is the streamwise distance between the center axes of two neighboring VAWTs in the same column and ΔL_y is the spanwise distance between the center axes of two neighboring VAWTs in the same row. For each of the three VAWT types, three different turbine spacings are considered, i.e., $(S_x, S_y) = (10, 10)$, $(7, 5)$, and $(5, 5)$, for which the corresponding numbers of VAWT rows and columns included in the LES are $(N_{row}, N_{col}) = (7, 8)$, $(11, 16)$, and $(13, 16)$, respectively. These spacings are chosen based on the prior LES study of turbulent boundary

TABLE II. Key parameters of the VAWT array configurations.

Case	VAWT type	γ	S_x	S_y	N_{row}	N_{col}	No. of VAWTs
HN10D	Helical-bladed	-127°	10	10	7	8	56
S10D	Straight-bladed	0°	10	10	7	8	56
HP10D	Helical-bladed	127°	10	10	7	8	56
HN7D	Helical-bladed	-127°	7	5	11	16	176
S7D	Straight-bladed	0°	7	5	11	16	176
HP7D	Helical-bladed	127°	7	5	11	16	176
HN5D	Helical-bladed	-127°	5	5	13	16	208
S5D	Straight-bladed	0°	5	5	13	16	208
HP5D	Helical-bladed	127°	5	5	13	16	208

layer flows interacting with arrays of straight-bladed VAWTs.¹⁷ Note that the intermediate spacing $(S_x, S_y) = (7, 5)$ is also close to those considered in previous LES studies of wind farms flows for HAWTs.^{26–28,32,33} In all the reported simulation cases, the center axis of the first VAWT in the array (i.e., the one in the first row and the first column) is located at $(x_1, y_1) = (7.2, 4.5) \text{ m} = (4D, 2.5D)$. Figure 2 shows an illustration of the 3D flow field for case HN5D obtained from the current LES.

In both the precursor and the main simulation domains, the bottom boundary is set to be flat with a surface roughness of $z_0 = 0.01 \text{ m}$ [used in the wall model Eq. (3)], which falls within the range of the values of $z_0 = O(0.001) \sim O(1) \text{ m}$ typically used in LES of atmospheric boundary layer turbulence over flat terrains.^{49,53,69,70} The flow in the precursor domain is driven by a prescribed streamwise pressure gradient force as shown in Eq. (2), i.e., $f_p = -dp_\infty/dx$. When the simulated flow in the precursor domain reaches the fully developed statistically steady state, the corresponding wind friction velocity is $u_* = \sqrt{-(L_z/\rho)dp_\infty/dx} = 0.64 \text{ m/s}$ and the mean wind velocity (obtained by time and horizontal planar averaging) at the VAWT equator height is $U_{eq} = 11.36 \text{ m/s}$. In the main simulation domain, the flow is driven by the inflow fed into the simulation domain at the $x = 0$ boundary, and no streamwise force is imposed, i.e., $f_p = 0$.

The precursor simulation domain is discretized using $920 \times 920 \times 300$ grid points, and the main simulation domain is discretized using $1058 \times 920 \times 300$ grid points. These computational grid points are evenly spaced in each direction, yielding identical grid resolutions of $(\Delta x, \Delta y, \Delta z) = (0.157, 0.157, 0.067) \text{ m}$ in both simulation domains. The computational mesh used in this study is illustrated in the close-up view of the (x, z) -plane around the first VAWT in Fig. 1. The size of the Gaussian kernel for the ALM (see Appendix A for details) is set to be $\varepsilon = 0.160 \text{ m}$. This kernel size yields $\varepsilon/\Delta \approx 1.36$, where $\Delta = (\Delta x \Delta y \Delta z)^{1/3} \approx 0.118 \text{ m}$, to ensure good numerical stability when applying the distributed turbine force $f_{e,i}$ in the LES solver.^{24,38,40,41} Meanwhile, this kernel size yields a ratio of $\varepsilon/c = 0.31$, which is close to the optimal kernel width criterion [i.e., $\varepsilon/c \sim O(0.4)$] reported in Martínez-Tossas *et al.*⁷¹ Overall, the LES parameters used in this study are similar to those used in Gharaati *et al.*²⁴ The simulations were run using a constant time step of $\Delta t = 6.25 \times 10^{-4} \text{ s}$, which is adequate to capture the effects of rotating VAWTs on the wind flow as it corresponds to about 600–800 time steps per rotation

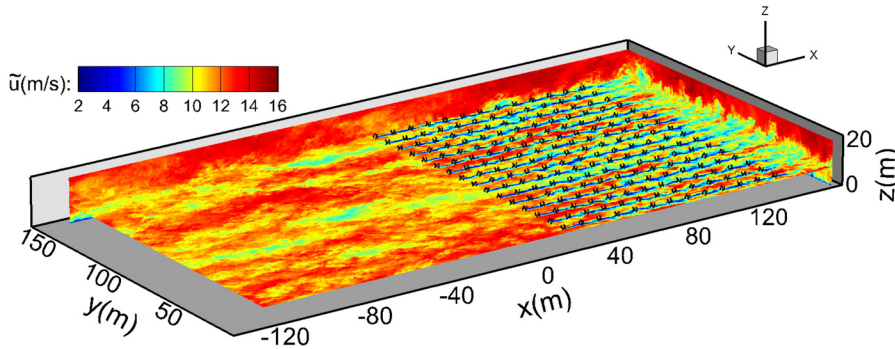


FIG. 2. Illustration of instantaneous flow field obtained from LES case HN5D. The precursor simulation domain occupies $x \in [-144, 0]$ m, and the main simulation domain with 13×16 helical VAWTs occupies $x \in [0, 165.6]$ m with the fringe zone at $x \in [144.9, 165.6]$ m. Contours of \tilde{u} are shown on the two vertical planes and the horizontal plane at the VAWT equator height $z = z_{eq}$.

for the VAWTs modeled in the present study. For each case, the simulation was run for about 630 s (i.e., about 50 times of the flow through time estimated based on L_x^p/U_{eq}) to allow the simulated flow field reach the statistically steady state. After then, the simulation was continued for another 50 s duration, from which 4000 instantaneous snapshots of the flow field with a constant time interval of 0.0125 s were sampled to calculate the time-average statistics of the simulated flow.

IV. RESULTS

As illustrated in Figs. 2 and 3, the turbulent flow exhibits complex interactions with the large array of VAWTs. To characterize the flow physics and understand the effects of VAWT blade geometry, in this section the LES results are analyzed by studying the close-up view of the instantaneous flow field around a small subset of the VAWT array (Sec. IV A) as well as by analyzing various flow statistics of the entire array (Secs. IV B–IV E).

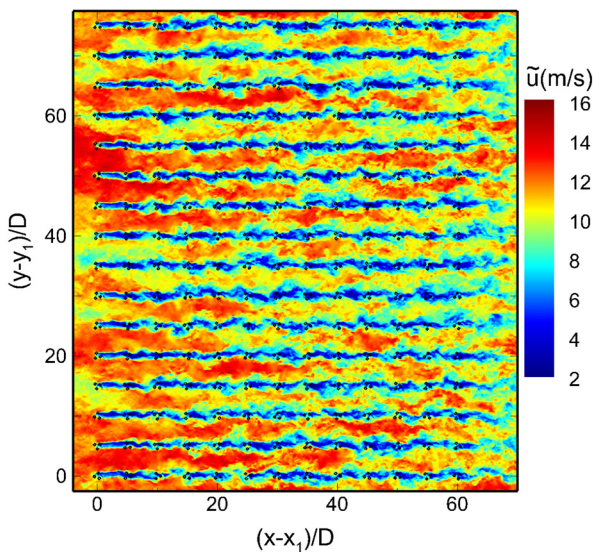


FIG. 3. Top view of the instantaneous flow field in the array of 13×16 helical VAWTs in case HN5D. The contours of the streamwise velocity \tilde{u} are shown on the (x, y) -plane at the VAWT equator height $z = z_{eq}$. The instantaneous cross-sectional locations of the VAWT blades are indicated by the small black circles.

A. Instantaneous velocity fields

Figure 4 shows the close-up views of the instantaneous flow fields around the first four VAWTs in the second column of the array for cases S10D and HN10D. In both cases, the flow characteristics in the near-wake region of the first VAWT resemble those reported in Gharaati *et al.*²⁴ based on LES of single VAWTs (i.e., without any downstream VAWT). In particular, in case S10D, the streamwise velocity \tilde{u} in the near wake of the first VAWT exhibits vertical streak patterns due to the drag effect induced by the rotating straight blades [see Fig. 4(b)], and the vertical velocity \tilde{w} exhibits turbine-induced fluctuations mainly in the two shear layers at the top and bottom edges of the VAWT wake due to shear instability [see Fig. 4(c)]. Differently, in case HN10D, the helical-shaped blades with $\gamma = -127^\circ$ generate inclined low-speed streaks of \tilde{u} behind the first VAWT [see Fig. 4(e)], where the vertical velocity \tilde{w} exhibits noticeable fluctuations also in the form of inclined streaks in the near wake [see Fig. 4(f)] due to the three-dimensional wake flow patterns induced by the helical-shaped blades.²⁴ Compared with case HN10D, in case HP10D [see Figs. 5(a) and 5(b)], the reversed twist direction of the helical blades results in reversed effects on the inclination direction of the streak patterns for \tilde{u} and \tilde{w} (for a more detailed comparison, see also Gharaati *et al.*²⁴).

Unlike the first VAWT in the column that faces the undisturbed boundary layer turbulence inflow, the downstream VAWTs experience inflow with higher turbulent intensity due to the wake effect of the upstream VAWTs, resulting in more intensive turbulent fluctuations in their wakes than that behind the first VAWT. The enhanced turbulent fluctuations due to wake-VAWT interactions are also affected by the spacing between VAWTs in the array. Figure 5 compares the side-views of the instantaneous flow fields in the arrays of $\gamma = 127^\circ$ helical VAWTs with three different spacings, i.e., cases HP10D, HP7D, and HP5D. The corresponding top views of the instantaneous flow field for these three cases are shown in Fig. 6. In case HP10D, the wake flow of each VAWT has adequate space to recover the wind speed and lower the turbulent intensity before reaching the downstream VAWT. As the streamwise spacing of the VAWTs reduces to $S_x = 7$ in case HP7D and $S_x = 5$ in case HP5D, wakes of the upstream VAWTs impact the downstream VAWTs when they still possess low wind speed and high-level turbulent fluctuations, which can impact the power production and induce fatigue load to the VAWTs located inside the large array. The top-views of the flow fields within the VAWT arrays shown in Fig. 6 (also see Fig. 2) also exhibit considerable spatial variations in the instantaneous flow fields along different VAWT columns in the array. As a result, it is difficult to compare the results from different

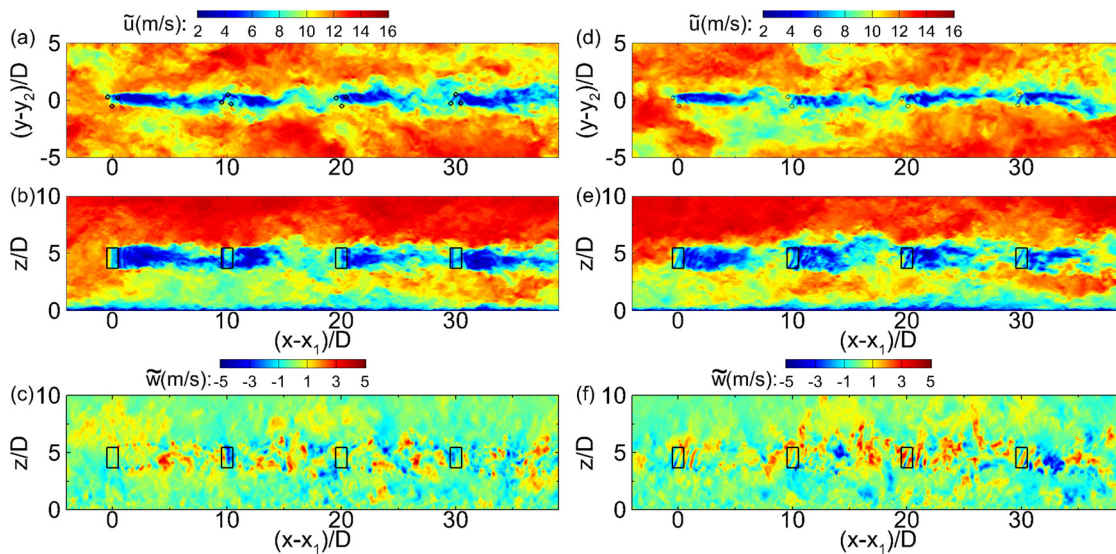


FIG. 4. Instantaneous velocity fields for cases S10D (left panels) and HN10D (right panels): (a) and (d) \tilde{u} on the (x,y) -plane at the VAWT equator height $z = z_{eq}$; (b) and (e) \tilde{u} on the (x,z) -plane across the centerline of the second column of the VAWT array, i.e., at $y = y_2$; and (c) \tilde{w} on the (x,z) -plane at $y = y_2$. In (a) and (d), the instantaneous cross-sectional locations of the VAWT blades are indicated using the small circles. In (b), (c), (e), and (f), the projected VAWT rotor regions are indicated using the rectangles.

simulation cases quantitatively by checking the instantaneous flow fields. In Secs. IV B–IV E, statistical analyses are conducted to provide more quantitative measures for the effects induced by different VAWT blade geometries under different array spacing conditions.

B. Mean flow field

As illustrated in Fig. 2, the simulated turbine array consists of a large number of VAWTs. The turbulent boundary layer flow produced by the precursor simulation also exhibits high-/low-speed streaks that

interact with different columns of VAWTs in the array. To obtain representative flow statistics, the ensemble average approach used in Gharati *et al.*²⁴ is adopted. First, time average is computed based on 4000 3D instantaneous snapshots of the entire flow field sampled between $t = 630$ and 680 s with a constant time interval of 0.0125 s between successive samples. Furthermore, the time-averaged flow field is evenly decomposed into N_{col} number of subdomains, each of which is centered along one column of VAWTs. The ensemble average of these N_{col} subdomains is conducted to further converge the statistics and average out the spatial variations caused by the low-/high-speed

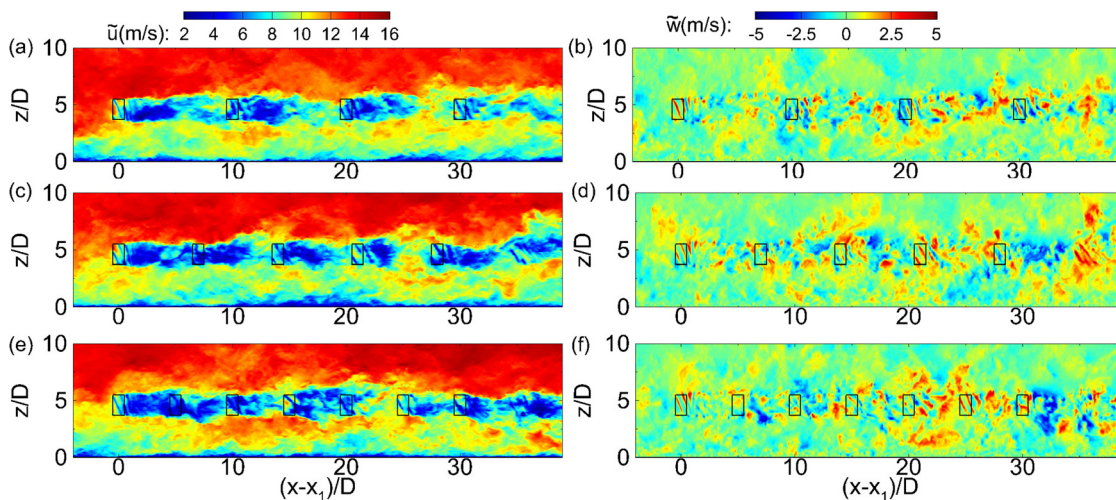


FIG. 5. Instantaneous flow fields in arrays of $\gamma = 127^\circ$ helical-bladed VAWTs with different spacings: (a) and (b) case HP10D, (c) and (d) case HP7D, and (e) and (f) case HP5D. The contours of the instantaneous streamwise velocity \tilde{u} (a), (c), and (e) and vertical velocity \tilde{w} (b), (d), and (f) are shown on the (x,z) -plane across the centerline of the second column of the VAWT array, i.e., at $y = y_2$. For each case, only a small fraction of the simulation domain is shown for illustration purposes.

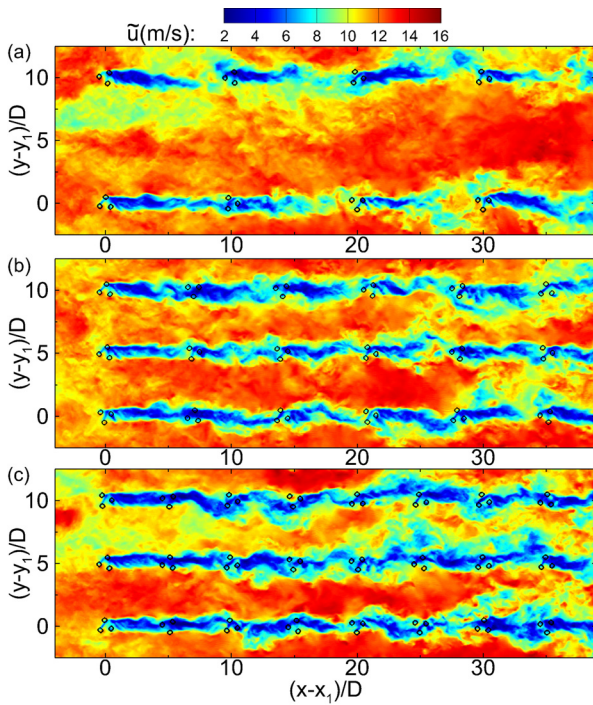


FIG. 6. Top-view of the instantaneous streamwise velocity fields in arrays of helical VAWTs of $\gamma = 127^\circ$ with different spacings: (a) case HP10D, (b) case HP7D, and (c) case HP5D. The contours of the streamwise velocity \tilde{u} are shown on the (x,y) -plane at the VAWT equator height $z = z_{eq}$. For each case, only a small fraction of the simulation domain is shown for illustration purposes.

streaks in the boundary layer turbulence. For an instantaneous flow quantity \tilde{f} obtained from the LES, its time average is denoted as \bar{f} and calculated as

$$\bar{f}(x, y, z) = \frac{1}{N_{ts}} \sum_{n=1}^{N_{ts}} \tilde{f}(x, y, z, t_n), \quad (5)$$

where N_{ts} is the total number of samples for time average and t_n is the corresponding time of the n th sample. The temporal fluctuation is defined as $f'(x, y, z, t) = \tilde{f}(x, y, z, t) - \bar{f}(x, y, z)$. The ensemble average of the time-averaged quantity is calculated based on

$$\langle \bar{f} \rangle(x, y', z) = \frac{1}{N_{col}} \sum_{j=1}^{N_{col}} \bar{f}(x, y' + (j-1)\Delta L_y, z) \quad \text{for } y' \in [0, \Delta L_y], \quad (6)$$

where $\Delta L_y = L_y/N_{col}$. Hereinafter, $\langle \bar{f} \rangle$ is referred to as the mean of \tilde{f} . As reported in Wei *et al.*¹⁹ and Gharaati *et al.*²⁴ based on the study of single VAWT's wake, an important effect induced by the helical-bladed VAWT is the mean vertical velocity in the wake flow. Here, this effect is further demonstrated in the VAWT array configuration. In particular, the comparison is made based on the three cases S10D, HN10D, and HP10D, which use the same $(S_x, S_y) = (10, 10)$ array configuration. The results from the other six cases for $(S_x, S_y) = (7, 5)$ and $(5, 5)$ exhibit qualitatively similar effect on the mean vertical

flow motion induced by the helical blades and, thus, are not shown here due to space limitations.

Figure 7 shows $\langle \bar{w} \rangle$ on the (x,z) -plane along the center of the averaged VAWT column for cases HN10D, S10D, and HP10D. Taking the straight-bladed VAWT case S10D [Fig. 7(b)] as the reference, the drag effect induced by the VAWT causes some of the wind flow to pass around the VAWT rotor from above and below, resulting in the positive/negative $\langle \bar{w} \rangle$ near the top/bottom ends of the VAWT rotor region, followed by negative/positive $\langle \bar{w} \rangle$ on the downstream side when the detoured wind reenters the wake region. For the two helical-bladed VAWT cases HN10D and HP10D [Figs. 7(a) and 7(c)], their mean vertical velocities $\langle \bar{w} \rangle$ exhibit noticeable differences from that in case S10D. For better illustration, the differences in $\langle \bar{w} \rangle$ between cases HN10D/HP10D and S10D are calculated, i.e., $\Delta \langle \bar{w} \rangle = \langle \bar{w} \rangle - \langle \bar{w} \rangle_s$, where $\langle \bar{w} \rangle_s$ is the mean vertical velocity of case S10D. The (x,z) - and (x,y) -plane views of $\Delta \langle \bar{w} \rangle$ are shown in Figs. 8 and 9, respectively.

For case HN10D with the $\gamma = -127^\circ$ helical VAWTs [Figs. 8(a) and 9(a)], the combination of the clockwise blade twist (from top to bottom) and the counterclockwise rotation of the VAWT causes the air flow to be pushed downward by the blades, resulting in a net downward flow near the spanwise edges of the wake region extended downstream from the blade surface, as indicated by the negative $\Delta \langle \bar{w} \rangle$ in the (x,y) -plane view shown in Fig. 9(a). This mean downward flow induced by the helical-shaped blades is balanced by the net upward flow along the center of the VAWT wake region, as indicated by the positive $\Delta \langle \bar{w} \rangle$ shown in Fig. 9(a). On the (x,z) -plane [Fig. 8(a)], this mean upward flow motion $\Delta \langle \bar{w} \rangle$ appears to dominate around the upper edge of the VAWT wake region. If the twist direction of the helical blades is reversed, as in case HP10D with the $\gamma = 127^\circ$ helical VAWTs, the sign and distribution pattern of $\Delta \langle \bar{w} \rangle$ also appear to be reversed [see Figs. 8(b) and 9(b)], which is consistent with the LES results reported in Gharaati *et al.*²⁴ Note that the VAWTs in the first row of the array face the undisturbed free-stream inflow. With the same TSR, these first-row VAWTs rotate faster than the VAWTs located inside the array, resulting in higher magnitude for $\Delta \langle \bar{w} \rangle$ in the

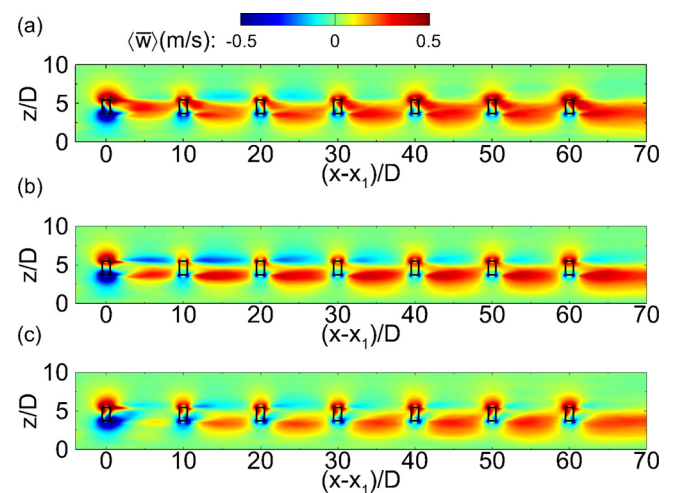


FIG. 7. Mean vertical velocity $\langle \bar{w} \rangle$ on the (x,z) -plane across the centerline of the VAWT column for (a) HN10D, (b) S10D, and (c) HP10D.

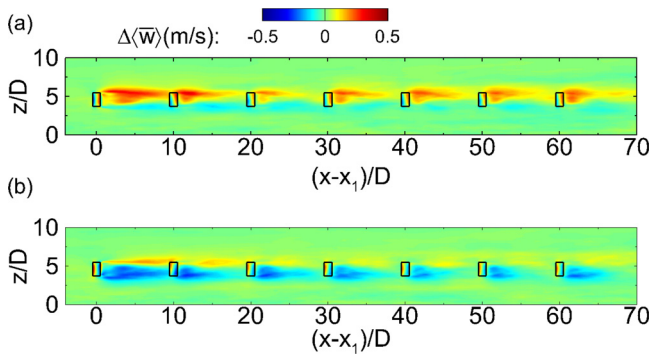


FIG. 8. Differences in the mean vertical velocity relative to case S10D, $\Delta\langle\bar{w}\rangle$: (a) case HN10D and (b) case HP10D. The contours are shown on the (x,z) -plane across the centerline of the VAWT column.

wake behind the first VAWT than those behind the downstream VAWTs (Figs. 8 and 9). Nevertheless, the mean vertical flow effect induced by the helical-bladed VAWTs persists through the entire VAWT array to affect the flow statistics.

A direct consequence of the helical-blade-induced vertical motion is the vertical tilting of the streamwise velocity deficit region behind the VAWT. Figures 10–12 show the contours of $\langle\bar{u}\rangle$ on the (x,z) -plane across the center of the VAWT column for all the nine simulation cases. The corresponding vertical profiles of $\langle\bar{u}\rangle$ extracted at $(x - x_1)/D = 3$ and 39 from Fig. 10 (i.e., cases HN10D, S10D, and HP10D) and Fig. 12 (i.e., cases HN5D, S5D, and HP5D) are shown in Fig. 13. In particular, the $(x - x_1)/D = 3$ location is chosen because it is at the same downstream distance from the first-row VAWTs for both the $(S_x, S_y) = (10, 10)$ and $(5, 5)$ array configurations; and the $(x - x_1)/D = 39$ location is chosen because it is at the same upstream distance in front of the fifth row for the $(S_x, S_y) = (10, 10)$ cases and the ninth row for the $(S_x, S_y) = (5, 5)$ cases.

The effect of the vertical flow motions induced by the helical-bladed VAWTs can be seen from Fig. 13(a) as well as from the contours of $\langle\bar{u}\rangle$ behind the first VAWT shown in Figs. 10 and 12. The upward/downward mean flow motion along the center region of the wake causes the upward/downward tilting of the low- $\langle\bar{u}\rangle$ region, resulting in reduction of velocity gradient $|\partial\langle\bar{u}\rangle/\partial z|$ near the lower

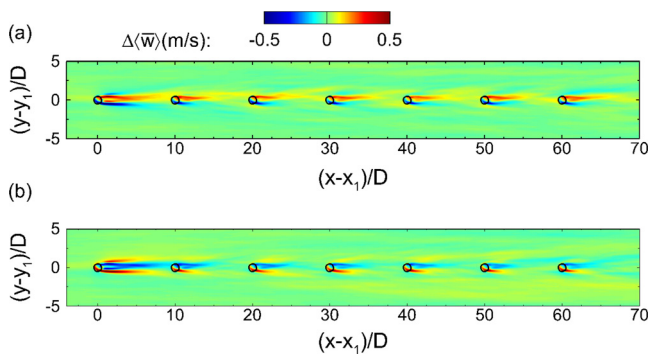


FIG. 9. Differences in the mean vertical velocity relative to case S10D, $\Delta\langle\bar{w}\rangle$: (a) case HN10D and (b) case HP10D. The contours are shown on the (x,y) -plane at the VAWT equator height $z = z_{eq}$.

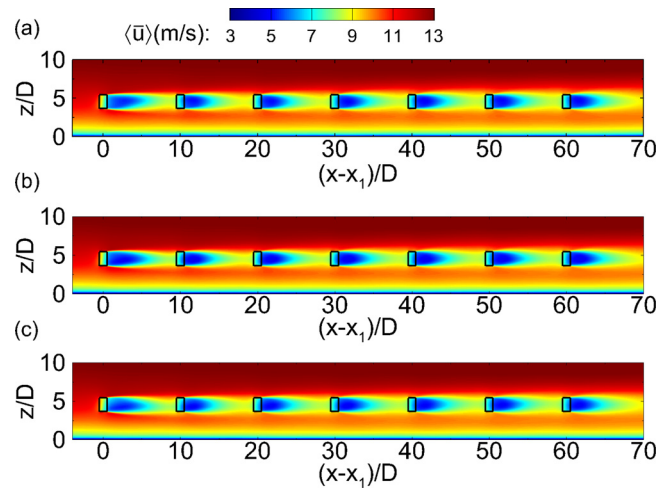


FIG. 10. Mean streamwise velocity $\langle\bar{u}\rangle$ on the (x,z) -plane across the centerline of the VAWT column for the cases with $S_x = 10$: (a) HN10D, (b) S10D, and (c) HP10D.

shear layer of the wake region for the cases with $\gamma = -127^\circ$ helical VAWTs [i.e., the two red color profiles in Fig. 13(a)] and near the upper shear layer for the cases with $\gamma = 127^\circ$ helical VAWTs [i.e., the two blue color profiles in Fig. 13(a)] when compared with the $\langle\bar{u}\rangle(z)$ profiles for the cases with the straight-bladed VAWTs [i.e., the two green color profiles in Fig. 13(a)]. For the simulation cases considered in this study, changing the VAWT spacings in the array appears to induce negligible effect on the velocity field behind the first-row VAWTs, as the velocity profiles of the corresponding cases with identical VAWT geometry overlap with each other [e.g., cases HN10D and HN5D in Fig. 13(a)]. Within the VAWT array, the mean velocity exhibits convergence toward a fully developed state after the VAWT row located around $(x - x_1)/D = 20$ (i.e., after the third row for cases with $S_x = 10$, the fourth row for cases with $S_x = 7$, and the fifth row for

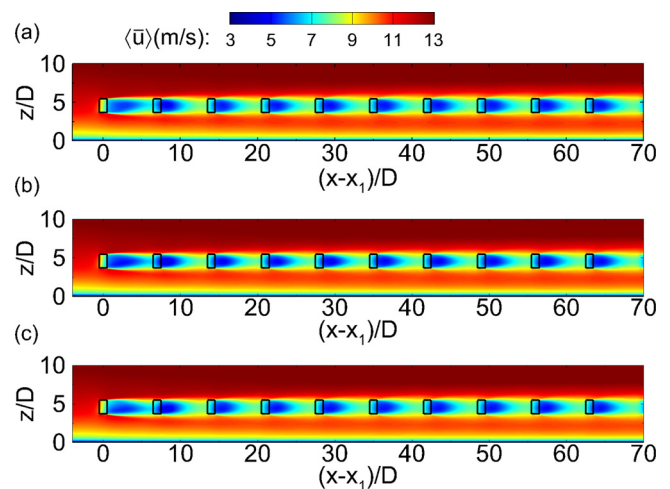


FIG. 11. Mean streamwise velocity $\langle\bar{u}\rangle$ on the (x,z) -plane across the centerline of the VAWT column for the cases with $S_x = 7$: (a) HN7D, (b) S7D, and (c) HP7D.

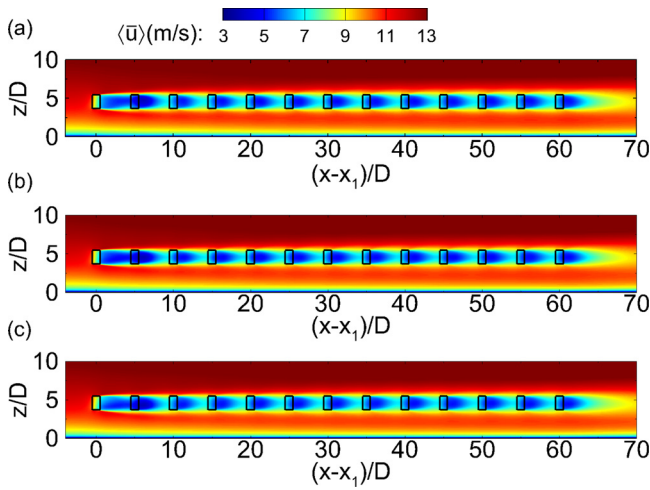


FIG. 12. Mean streamwise velocity $\langle \bar{u} \rangle$ on the (x,z) -plane across the centerline of the VAWT column for the cases with $S_x = 5$: (a) HN5D, (b) S5D, and (c) HP5D.

cases with $S_x = 5$) as indicated by the similarity in the $\langle \bar{u} \rangle$ contours further downstream as shown in Figs. 10–12. This convergence of VAWT array flow toward the fully developed state can also be seen from the downstream development of the VAWT power coefficient shown later in Sec. IV E. Similar fully developed state has been also reported in previous studies of finite-length wind turbine array flows based on HAWTs.^{29,30,72}

Figure 13(b) shows the representative $\langle \bar{u} \rangle(z)$ profiles for the inflow in front of VAWTs located in the fully developed region of the array. Reducing the streamwise spacing of the VAWTs can cause considerable reduction on the local inflow wind speed for VAWTs located inside the array. In particular, the mean streamwise velocity at the equator height [i.e., $\langle \bar{u} \rangle(z = z_{eq})$] can recover to about 75% of U_{eq} for the cases with $S_x = 10$ but can only recover to about 60% for the cases with $S_x = 5$. This difference in the mean wind speed for different spacings lead to differences in the mean power coefficient, which are discussed in Sec. IV E.

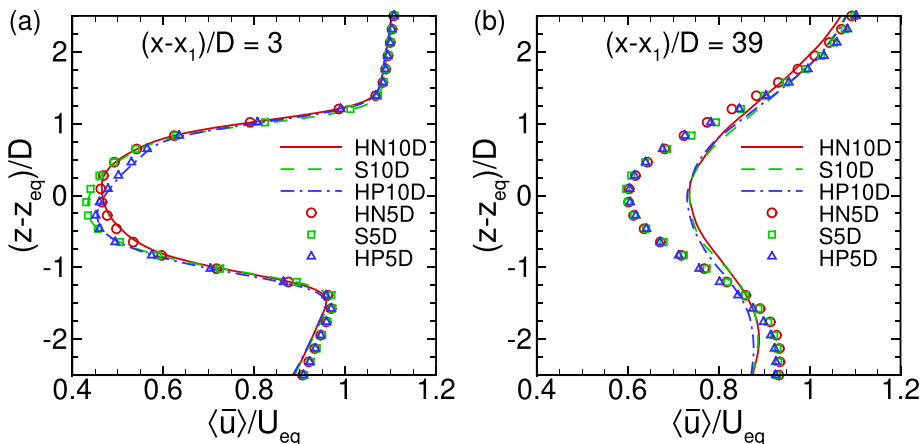


FIG. 13. Vertical profiles of mean streamwise velocity $\langle \bar{u} \rangle$ along the VAWT column centerline for cases with $S_x = 10$ and $S_x = 5$ at: (a) $(x - x_1)/D = 3$ and (b) $(x - x_1)/D = 39$. The symbols are plotted for every five vertical grid points.

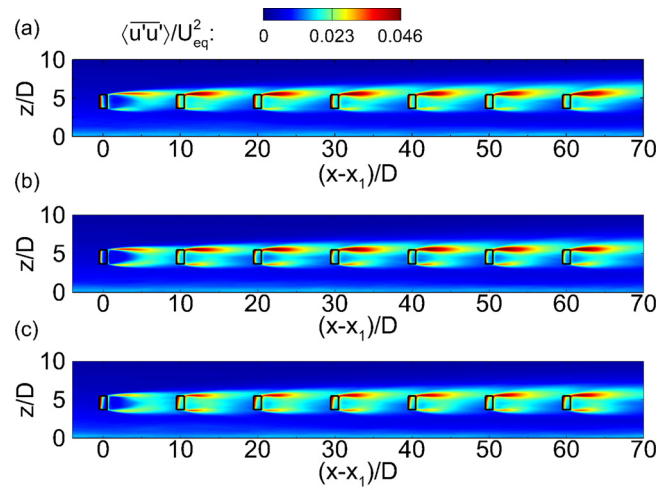


FIG. 14. Covariance of streamwise velocity $\langle \overline{u'u'} \rangle$ on the (x,z) -plane across the centerline of the VAWT column for cases with $S_x = 10$: (a) HN10D, (b) S10D, and (c) HP10D.

C. Turbulence statistics

Compared with VAWTs located in the first row, VAWTs located inside the array operate in a more complex wind field with reduced mean wind speed but increased turbulent fluctuations due to the VAWT wake effects. Turbulent fluctuations play an important role on entraining the kinetic energy into the VAWT array to supply the wind energy extraction.^{25–27,32,33} In this section, the turbulence statistics of the VAWT wakes in the large array are analyzed.

Figures 14 and 15 show the contours of $\langle \overline{u'u'} \rangle$ on the (x,z) -plane across the centerline of the VAWT column for the cases with $S_x = 10$ and 5, respectively, and Fig. 16 shows the corresponding vertical profiles at $(x - x_1)/D = 32$ and 39. Note that $(x - x_1)/D = 32$ is located at $2D$ downstream of the nearest VAWT (i.e., the third row for $S_x = 10$ and the seventh row for $S_x = 5$), and $(x - x_1)/D = 39$ is located at $1D$ upstream of the nearest VAWT (i.e., the fourth row for $S_x = 10$ and the ninth row for $S_x = 5$). Due to the vertical tilting of the VAWT wake caused by the mean vertical flow motion induced by the helical

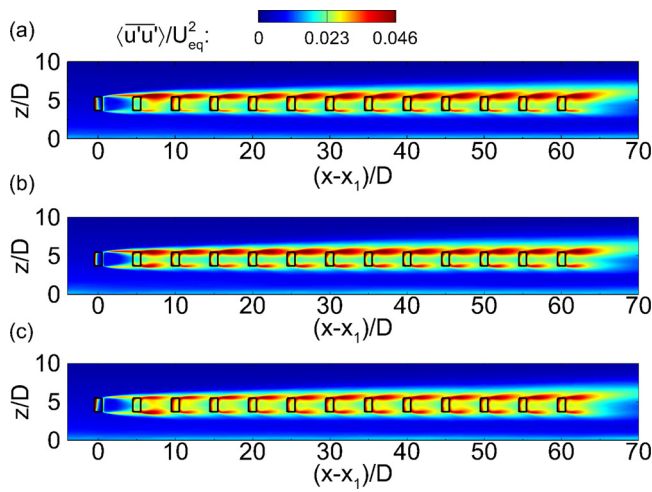


FIG. 15. Covariance of streamwise velocity $\langle \bar{u}'\bar{u}' \rangle$ on the (x,z) -plane across the centerline of the VAWT column for cases with $S_x = 5$: (a) HN5D, (b) S5D, and (c) HP5D.

blades (see Figs. 8 and 9), the intensity of the vertical gradient of $\langle \bar{u} \rangle$ is weakened near the lower (upper) shear layer of the wake behind the negative (positive) helical VAWT when compared with the corresponding straight-bladed VAWT case [see Fig. 13(a)]. This weakening effect on the velocity gradient results in the weakening of $\langle \bar{u}'\bar{u}' \rangle$. Taking as an example the $S_x = 10$ cases shown in Fig. 16(a), case HP10D exhibits smaller peak value of $\langle \bar{u}'\bar{u}' \rangle$ near $(z - z_{eq})/D = 1$ than case S10D, while case HN10D exhibits smaller peak value than case S10D near $(z - z_{eq})/D = -1$. Reducing the VAWT spacing causes the turbulence intensity in the near-wake region of the VAWTs to increase, but the overall effect of the helical blades appears to be qualitatively similar between the cases with $S_x = 10$ and 5 [see Fig. 16(a) vs Fig. 16(c)]. Reducing the streamwise spacing of VAWTs induces more significant effect on the inflow turbulence intensity of VAWTs, as shown in Figs. 16(b) and 16(d). With more streamwise spacing, the wake flow of the upstream VAWTs have more space/time to recover the speed and dissipate the turbulence fluctuation, which can lead to less fatigue load on the downstream VAWTs.

In the VAWT wake, the Reynolds shear stress tensor $\langle \bar{u}'_i \bar{u}'_j \rangle$ plays an important role on entraining momentum and kinetic energy from the surrounding high-speed flow into the wake region to recover the

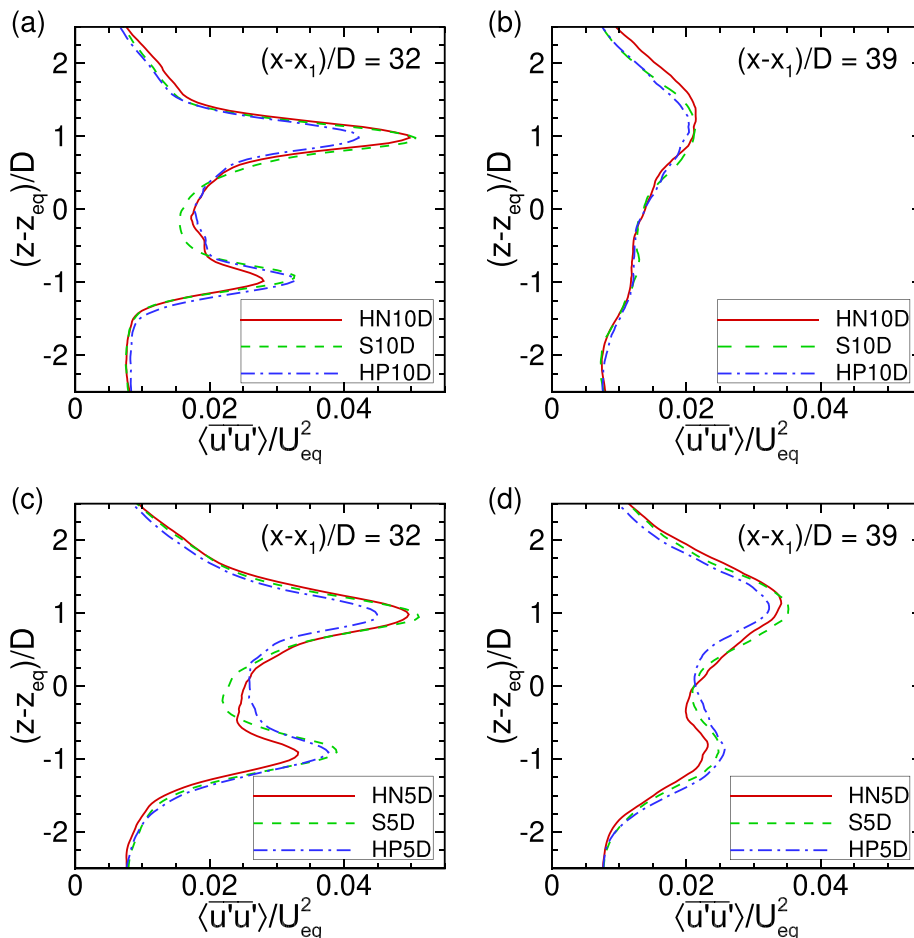


FIG. 16. Vertical profiles of $\langle \bar{u}'\bar{u}' \rangle$ across the VAWT column centerline at $(x - x_1)/D = 32$ (a) and (c) and $(x - x_1)/D = 39$ (b) and (d). Panels (a) and (b) are for $S_x = 10$, and panels (c) and (d) are for $S_x = 5$.

13 December 2023 16:30:34

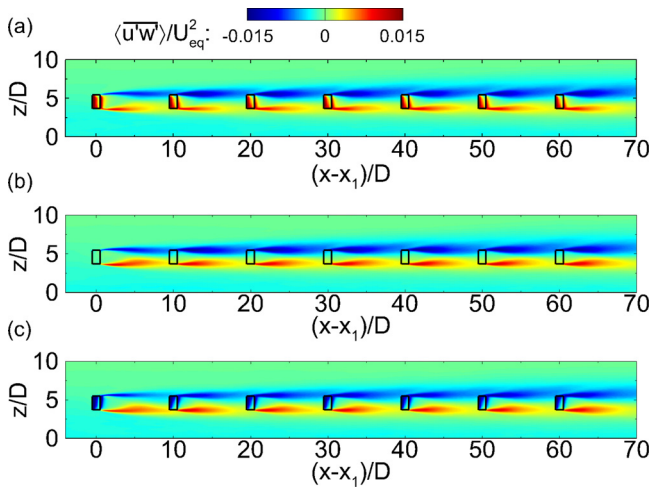


FIG. 17. Reynolds shear stress $\langle u'w' \rangle$ on the (x,z) -plane across the VAWT column centerline for the cases with $S_x = 10$: (a) HN10D, (b) S10D, and (c) HP10D.

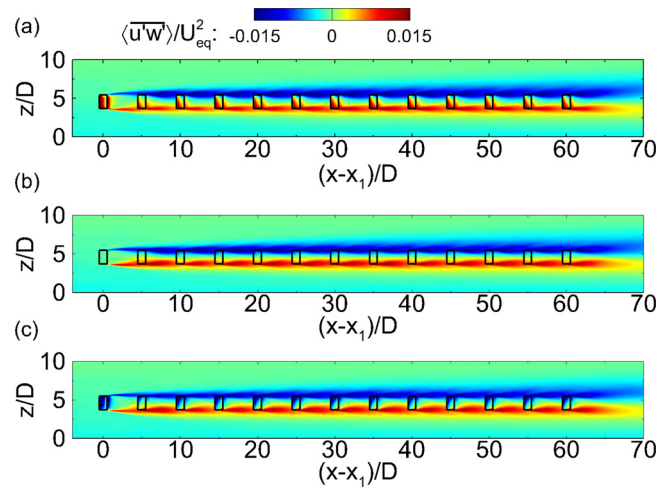


FIG. 18. Reynolds shear stress $\langle u'w' \rangle$ on the (x,z) -plane across the VAWT column centerline for the cases with $S_x = 5$: (a) HN5D, (b) S5D, and (c) HP5D.

wind speed. In particular, the turbulent entrainment of momentum is governed by $\langle u'w' \rangle$ in the vertical direction and by $\langle u'v' \rangle$ in the spanwise direction. Figures 17 and 18 show the contours of $\langle u'w' \rangle$ on the (x,z) -plane across the centerline of the VAWT column for the cases with $S_x = 10$ and 5, respectively. Figure 19 shows the corresponding vertical profiles of $\langle u'w' \rangle$ at $(x - x_1)/D = 33$ extracted from Figs. 17 and 18. Similar to the effects on $\langle u'u' \rangle$, the negative (positive) helical VAWT causes the weakening of $\langle u'w' \rangle$ near the lower (upper) shear layer compared with the corresponding straight-bladed VAWT case (Fig. 19). In the cases with $S_x = 10$ (Fig. 17), the intensity of $\langle u'w' \rangle$ exhibits noticeable variation as the wake flow travels through the 10D streamwise distance toward the downstream VAWT row. As the streamwise spacing is reduced to $S_x = 5$ (Fig. 18), $\langle u'w' \rangle$ remains at high-intensity level over the smaller 5D streamwise distance between VAWT rows, forming two continuous shear layers around the upper and lower edges of the VAWT rotor region that are overall stronger than the two shear layers in the corresponding cases with $S_x = 10$ (Fig. 17). As shown later in Sec. IV D, the enhanced overall $\langle u'w' \rangle$

intensity (due to less streamwise variation) results in more turbulent entrainment of kinetic energy to supply the wind power extraction by more VAWTs in the $S_x = 5$ cases.

Figures 20 and 21 show the contours of $\langle u'v' \rangle$ on the (x,y) -plane at the VAWT equator height $z = z_{eq}$ for the cases with $S_x = 10$ and 5, respectively, and Fig. 22 shows the corresponding spanwise profiles of $\langle u'v' \rangle$ extracted at $(x - x_1)/D = 33$. Similar to the effect on $\langle u'w' \rangle$, reducing the streamwise spacing from $S_x = 10$ to 5 leaves less space for $\langle u'v' \rangle$ to decay before reaching the successive downstream VAWTs, forming two continuous lateral shear layers aside the VAWT column with strong turbulent entrainment. Moreover, Fig. 22 shows that the wakes of the two helical-bladed VAWTs exhibit higher magnitude of $\langle u'v' \rangle$ than the straight-bladed VAWT near $(y - y_1)/D = -0.5$, which can lead to more lateral turbulent entrainment of momentum and kinetic energy.

Here, the shear-induced production of $\langle u'v' \rangle$ is analyzed to help understand the difference caused by the VAWT blade geometry. The

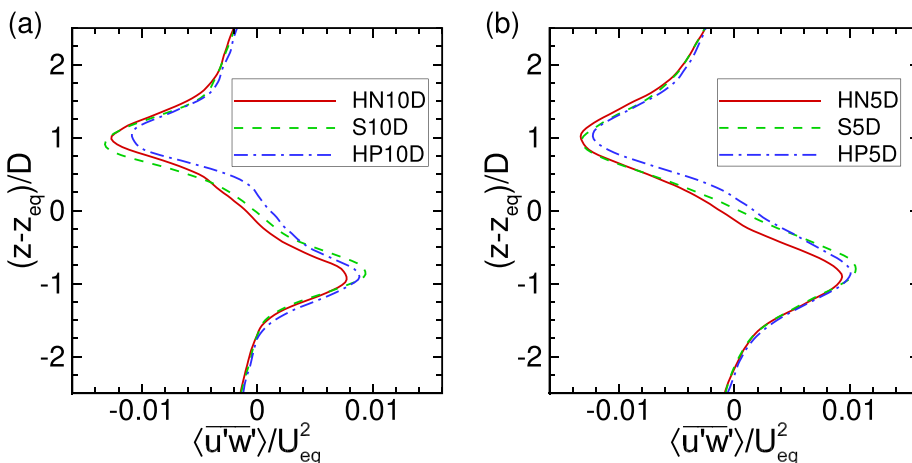


FIG. 19. Vertical profiles of $\langle u'w' \rangle$ across the VAWT column centerline at $(x - x_1)/D = 33$. Panel (a) shows the cases with $S_x = 10$, and panel (b) shows the cases with $S_x = 5$.

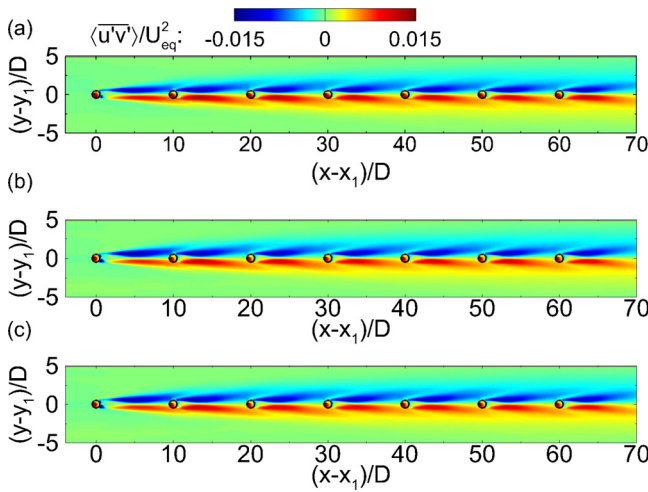


FIG. 20. Reynolds shear stress $\langle u'v' \rangle$ on the (x,y) -plane at the VAWT equator height $z = z_{eq}$ for the cases with $S_x = 10$: (a) HN10D, (b) S10D, and (c) HP10D.

transport equation for the Reynolds shear stress component $\langle u'v' \rangle$ in the VAWT wake can be written as [see Eq. (7.178) in Pope⁷³]

$$0 = -\frac{\partial \langle u'v' \rangle}{\partial t} - \langle \bar{u}_j \rangle \frac{\partial \langle u'v' \rangle}{\partial x_j} - \underbrace{\langle \bar{u}'u'_j \rangle \frac{\partial \langle \bar{v} \rangle}{\partial x_j} - \langle \bar{v}'u'_j \rangle \frac{\partial \langle \bar{u} \rangle}{\partial x_j}}_{P_{12}} - \frac{1}{\rho} \underbrace{\langle u' \frac{\partial p'}{\partial y} + v' \frac{\partial p'}{\partial x} \rangle}_{\Pi_{12}} - \underbrace{\frac{\partial \langle u'v'u'_j \rangle}{\partial x_j}}_{T_{12}} + \nu \underbrace{\frac{\partial^2 \langle u'v' \rangle}{\partial x_j^2}}_{D_{12}^{\nu}} + \underbrace{\frac{\partial}{\partial x_j} \langle \nu_{sgs} \frac{\partial \langle u'v' \rangle}{\partial x_j} \rangle}_{D_{12}^{sgs}} - 2\nu \underbrace{\langle \frac{\partial u'}{\partial x_j} \frac{\partial v'}{\partial x_j} \rangle}_{\epsilon_{12}^{\nu}} - 2 \underbrace{\langle \nu_{sgs} \frac{\partial u'}{\partial x_j} \frac{\partial v'}{\partial x_j} \rangle}_{\epsilon_{12}^{sgs}}, \quad (7)$$

where P_{12} is the total production of $\langle u'v' \rangle$ caused by the shear instability, Π_{12} is the velocity–pressure-gradient tensor, T_{12} is the transport

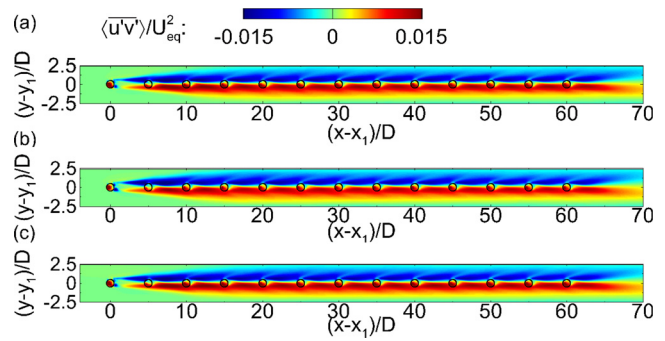


FIG. 21. Reynolds shear stress $\langle u'v' \rangle$ on the (x,y) -plane at the VAWT equator height $z = z_{eq}$ for the cases with $S_x = 5$: (a) HN5D, (b) S5D, and (c) HP5D.

due to resolved turbulence, D_{12}^{ν} is the molecular diffusion, D_{12}^{sgs} is the SGS diffusion, ϵ_{12}^{ν} is the molecular dissipation, and ϵ_{12}^{sgs} is the SGS dissipation.

Figure 23 shows the contours of $\langle u'v' \rangle$ and its production P_{12} on the (y,z) -plane at $(x - x_1)/D = 33$ for the three cases with $S_x = 10$. The results for $S_x = 5$ are qualitatively similar and, thus, are not shown here due to space limitation. The distributions of $\langle u'v' \rangle$ and P_{12} exhibit strong correlation. Both of them exhibit higher magnitude in the shear layer around $(y - y_1)/D = -0.5$ in the two helical-bladed VAWT cases than in the straight-bladed VAWT case, which is consistent with the results shown in Fig. 22(a). Note that P_{12} can be expressed in six separate terms as

$$P_{12} = \underbrace{-\langle \bar{u}'u' \rangle \frac{\partial \langle \bar{v} \rangle}{\partial x}}_{P_{12}^b} - \underbrace{\langle \bar{u}'v' \rangle \frac{\partial \langle \bar{v} \rangle}{\partial y}}_{P_{12}^p} - \underbrace{\langle \bar{u}'w' \rangle \frac{\partial \langle \bar{v} \rangle}{\partial z}}_{P_{12}^c} - \underbrace{\langle \bar{v}'u' \rangle \frac{\partial \langle \bar{u} \rangle}{\partial x}}_{P_{12}^d} - \underbrace{\langle \bar{v}'v' \rangle \frac{\partial \langle \bar{u} \rangle}{\partial y}}_{P_{12}^e} - \underbrace{\langle \bar{v}'w' \rangle \frac{\partial \langle \bar{u} \rangle}{\partial z}}_{P_{12}^f}. \quad (8)$$

For the current VAWT wake flow problem, P_{12}^b , P_{12}^d , and P_{12}^e are the dominant terms, among which P_{12}^b and P_{12}^d have opposite signs

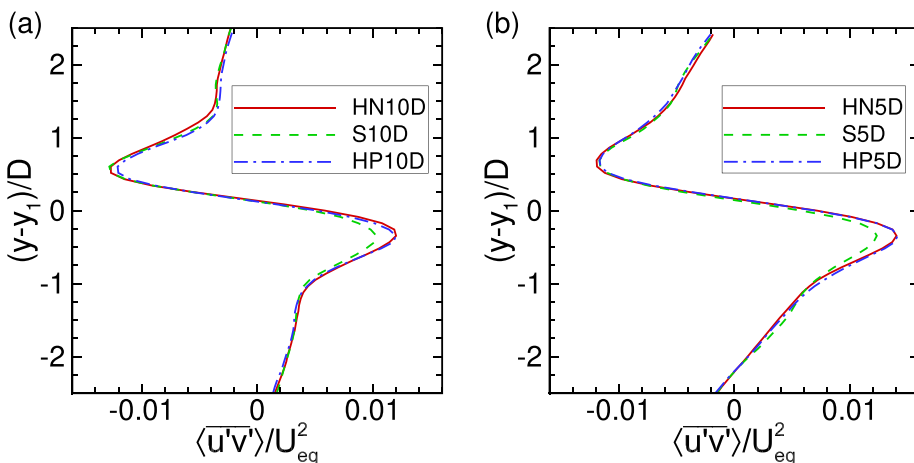


FIG. 22. Spanwise profiles of $\langle u'v' \rangle$ at the VAWT equator height $z = z_{eq}$ at the streamwise location $(x - x_1)/D = 33$. Panel (a) shows the cases with $S_x = 10$, and panel (b) shows the cases with $S_x = 5$.

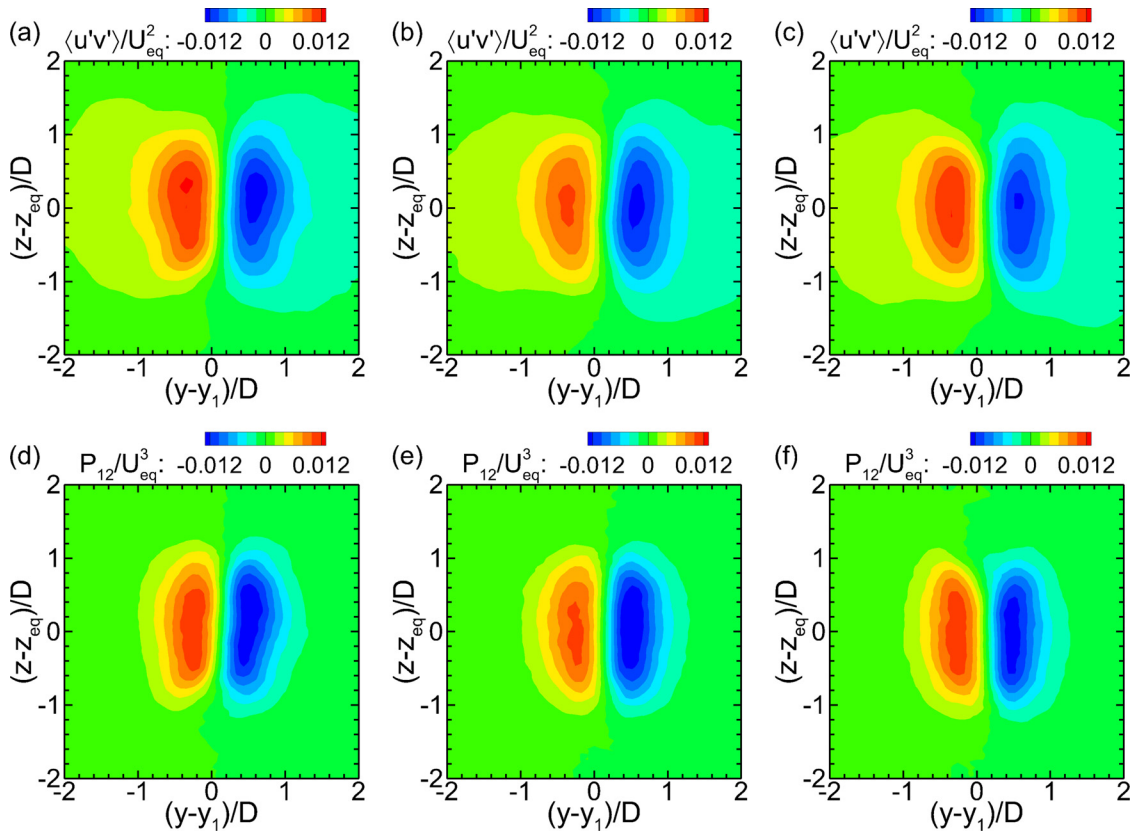


FIG. 23. Reynolds shear stress $\langle u'v' \rangle$ (a)–(c) and its production P_{12} (d)–(f) on the (y,z) -plane at $(x - x_1)/D = 33$ for the cases with $S_x = 10$: (a) and (d) case HN10D, (b) and (e) case S10D, and (c) and (f) case HP10D.

(thus leading to considerable cancellation) and are about one order of magnitude smaller than P_{12}^e . Therefore, the total production P_{12} is dominated by the contribution from $P_{12}^e = -\langle v'v' \rangle (\partial \langle \bar{u} \rangle / \partial y)$. As shown in Fig. 24, the spanwise profiles of $\langle \bar{u} \rangle$ are similar for the cases with different VAWTs, resulting in similar values for $\partial \langle \bar{u} \rangle / \partial y$. Thus, the differences in P_{12} are mainly due to $\langle v'v' \rangle$. Figure 25 compares the

distributions of $\langle v'v' \rangle$ on the (y,z) -plane at $(x - x_1)/D = 33$ for the three cases with $S_x = 10$. Compared with the straight-bladed case S10D, the high-intensity region of $\langle v'v' \rangle$ in cases HN10D and HP10D extend more toward the $(y - y_1) < 0$ half of the plane. The combination of similar value of $\partial \langle \bar{u} \rangle / \partial y$ with higher value of $\langle v'v' \rangle$ in the shear layer at $(y - y_1) < 0$ in the helical VAWT cases (HN10D and

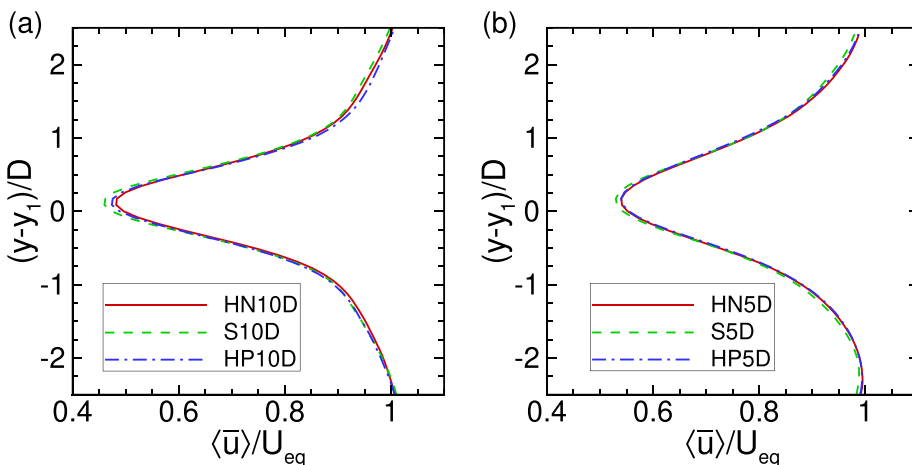


FIG. 24. Spanwise profiles of $\langle \bar{u} \rangle$ at the VAWT equator height $z = z_{eq}$ at the streamwise location $(x - x_1)/D = 33$. Panel (a) shows the cases with $S_x = 10$, and panel (b) shows the cases with $S_x = 5$.

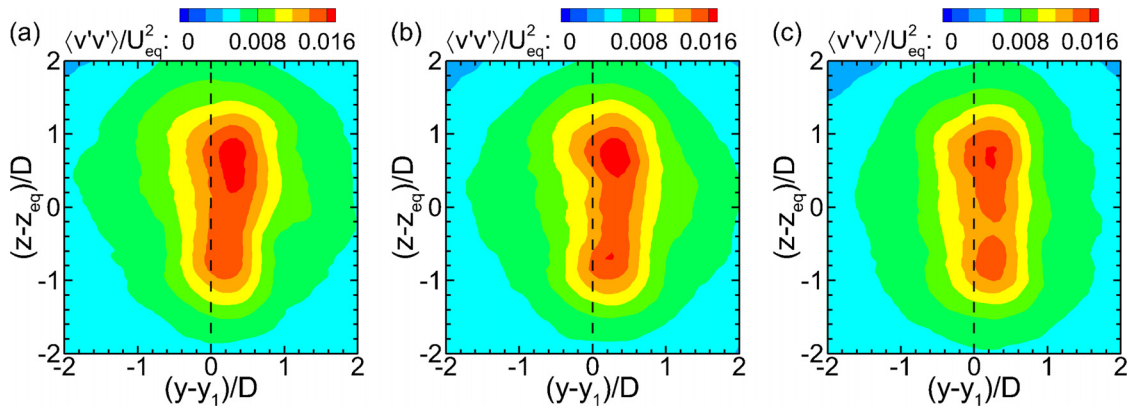


FIG. 25. Covariance of spanwise velocity $\langle v'v' \rangle$ on the (y,z) -plane at $(x - x_1)/D = 33$ for the cases with $S_x = 10$: (a) case HN10D, (b) case S10D, and (c) case HP10D.

HP10D) results in the higher production P_{12} than that in case S10D, producing higher magnitude of $\langle u'v' \rangle$ in this region as shown in Fig. 23.

D. Transport tube of mean kinetic energy

To visualize the energy transport in array of VAWTs, here the transport-tube method developed by Meyers and Meneveau⁷⁴ is adopted. In particular, the transport of mean kinetic energy ($K = \langle \bar{u}_i \rangle \langle \bar{u}_i \rangle / 2$) is governed by the following equation:

$$\frac{\partial F_{K,j}}{\partial x_j} = -\frac{1}{\rho} \frac{\partial (\langle \bar{u}_i \rangle \langle \bar{p} \rangle)}{\partial x_i} + \langle \bar{u}'_i \bar{u}'_j \rangle \frac{\partial \langle \bar{u}_i \rangle}{\partial x_j} + \langle \bar{\tau}_{ij}^{sgs} \rangle \langle \bar{S}_{ij} \rangle - \langle \bar{u}_i \rangle \frac{\langle \bar{f}_{e,i} \rangle}{\rho}, \quad (9)$$

where

$$F_{K,j} = K \langle \bar{u}_j \rangle + \langle \bar{u}'_i \bar{u}'_j \rangle \langle \bar{u}_i \rangle + \langle \bar{\tau}_{ij}^{sgs} \rangle \langle \bar{u}_i \rangle \quad (10)$$

is the mean kinetic energy flux vector field per unit mass. The four terms on the right-hand side of Eq. (9) represent the pressure transport, the mean-shear induced production, the SGS dissipation of the mean kinetic energy, and the work done by the turbine force, respectively. Based on $F_{K,j}$, the transport velocity for the mean kinetic energy can be determined based on

$$\langle \bar{u}_{K,j} \rangle \equiv F_{K,j} / K = \langle \bar{u}_j \rangle + \langle \bar{u}'_i \bar{u}'_j \rangle \langle \bar{u}_i \rangle / K + \langle \bar{\tau}_{ij}^{sgs} \rangle \langle \bar{u}_i \rangle / K, \quad (11)$$

where the three terms on the right-hand side of Eq. (11) represent the contributions from the mean-flow advection, the resolved turbulent transport, and the unresolved SGS transport, respectively.

Following Meyers and Meneveau,⁷⁴ a transport tube of K is defined as a tubular region surrounded by the streamlines of the K -transport velocity $\langle \bar{u}_{K,j} \rangle$ in analogy to the concept of a stream tube for mass transport. In the current analysis, the transport tube of mean kinetic energy is constructed based on the streamlines of $\langle \bar{u}_{K,j} \rangle$ traced backwards (i.e., toward the upstream direction) from 120 evenly spaced starting points on the rectangular mantle of the projected VAWT rotor area at $(x - x_1)/D = 38.5$. Figure 26(a) shows the 3D illustration of the mean kinetic energy transport tube based on case HN10D. To show the effect of VAWT blade geometry on the kinetic

energy transport, three representative streamwise locations are chosen for comparison, i.e., $(x - x_1)/D = 31, 21,$ and 11 . The cross-sectional shapes of the tube mantle of cases HN10D, S10D, and HP10D at these three streamwise locations are shown in Figs. 26(b)–26(d) for comparison. In all three cases, the tube cross section exhibits noticeable expansion when traced upstream, indicating the entrainment of kinetic energy into the VAWT wake region to recover the wind speed.

As shown in Sec. IV C, the straight-bladed VAWT case S10D has stronger vertical turbulent entrainment $\langle u'w' \rangle$ but weaker spanwise turbulent entrainment flux $\langle u'v' \rangle$ than the other two helical-bladed VAWT cases. As a result, the tube mantle in case S10D shows more vertical expansion and less spanwise expansion than cases HN10D and HP10D (Fig. 26). In case HN10D [Fig. 26(b)], the vertical expansion of the tube mantle is dominated by the effect of $\langle u'w' \rangle$ and the helical-blade-induced mean upward flow. Relative to case S10D, in case HN10D the mean upward relative velocity $\Delta \langle \bar{w} \rangle$ near the upper side of the wake region [see Fig. 8(a)] partially cancels the downward turbulent entrainment effect of $\langle u'w' \rangle$, resulting in reduced vertical expansion of the tube's upper side as traced upstream [see Fig. 26(b) vs Fig. 26(c)]. On the other hand, in case HN10D, the tube expansion on the lower side is weakened due to the weakened $\langle u'w' \rangle$ [see Fig. 19(a)]. Similar to the effects on other turbulence statistics, reversing the blade twist direction of the helical-bladed VAWT causes the effects on the vertical expansion of the mean kinetic energy transport tube to be also reversed, as illustrated by the comparison between Figs. 26(b) and 26(d).

To illustrate the effects of VAWT spacing on the mean kinetic energy transport, the (y,z) -plane cross sections of the K transport tubes at $(x - x_1)/D = 31, 21,$ and 11 for cases HN10D and HN5D are shown in Fig. 27 for comparison. As discussed in Sec. IV C, reducing the streamwise spacing of the VAWT array causes the magnitudes of $\langle u'w' \rangle$ and $\langle u'v' \rangle$ in case HN5D to maintain at a higher intensity level than those in case HN10D, resulting in more turbulent entrainments of mean kinetic energy. This effect is reflected in the more expansion of the transport tube of case HN5D than case HN10D. The comparisons between other corresponding $S_x = 5$ and 10 cases exhibit consistent effect and, thus, are not shown here due to space limitation.

The differences in the transport of mean kinetic energy in the wake regions behind different types of VAWTs can cause different wind speed recovery that can impact the power production of the

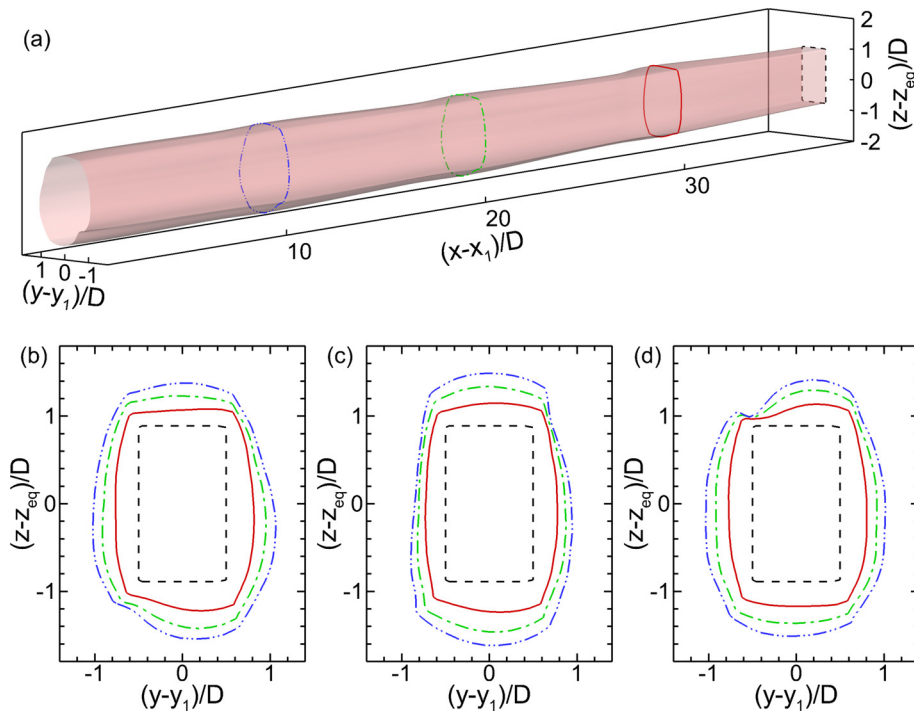


FIG. 26. Mean kinetic energy transport tubes for cases with $S_x = 10$. Panel (a) shows the three-dimensional visualization of the tube for case HN10D. Panels (b)–(d) show the (y,z) -plane views of the tube mantle at $(x - x_1)/D = 38.5$ (black dashed line), 31 (red solid line), 21 (green dashed-dotted line), and 11 (blue dashed-dotted-dotted line): (b) case HN10D, (c) case S10D, and (d) case HP10D.

downstream VAWTs. It should be noted that when a downstream VAWT extracts wind energy, its obstacle effect causes the increase in the pressure in front of the VAWT rotor that can affect the comparison of the wind speed recoveries between different simulation cases. That is to say, the inflow speed in front of a VAWT inside the array is the consequence of the combined effect of upstream VAWT wake recovery and the wind energy extraction (i.e., through the aerodynamic forces) of this downstream VAWT itself. To isolate the effect of wake

recovery for a fair comparison, the wake of the last VAWT row is chosen for analysis. The last row possesses similar inflow characteristics as other VAWT rows inside the fully developed region of the VAWT array, but does not have another downstream VAWT row to induce additional pressure effect.

Figure 28 compares the (y,z) -plane distributions of the mean streamwise velocity $\langle \bar{u} \rangle$ for the three $S_x = 10$ cases HN10D, S10D, and HP10D. The effects shown by the mean kinetic energy transport tubes

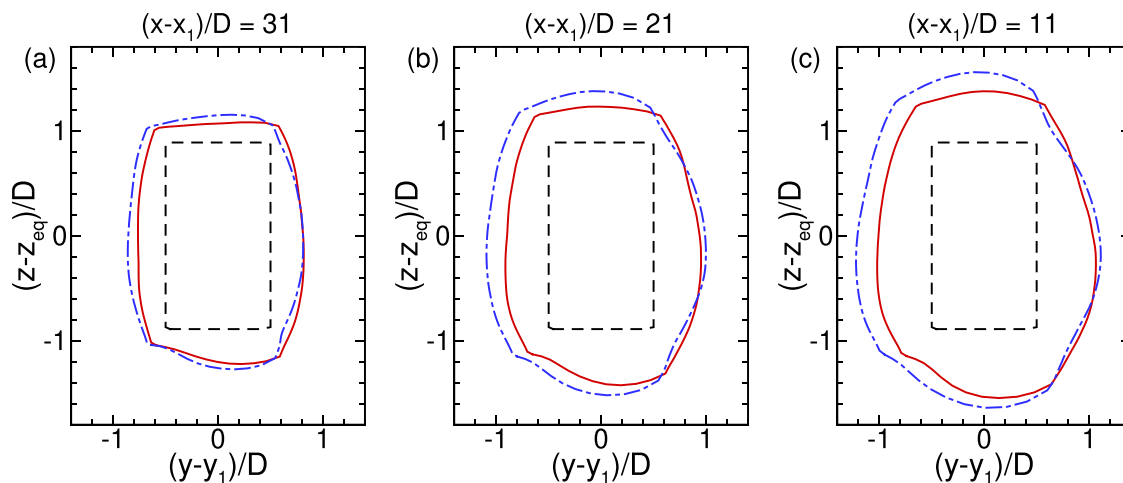


FIG. 27. Comparison of mean kinetic energy transport tubes between cases HN10D and HN5D. The figure shows the (y,z) -plane views of the tube mantle at different stream-wise locations $(x - x_1)/D =$: (a) 31, (b) 21, and (c) 11. In each panel, the black dashed line shows the initial rectangular tube mantle prescribed at $(x - x_1)/D = 38.5$, the red solid line is for case HN10D, and the blue dashed-dotted line is for case HN5D.

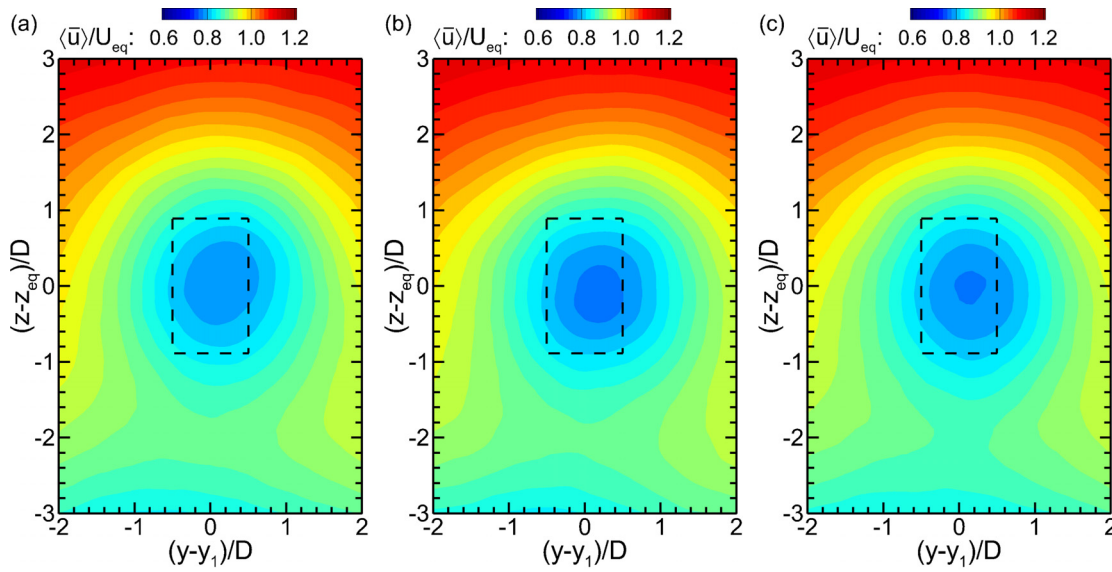


FIG. 28. Mean streamwise velocity $\langle \bar{u} \rangle$ on the (y, z) -plane at $(x - x_1) / D = 69$ for the cases with $S_x = 10$: (a) case HN10D, (b) case S10D, and (c) case HP10D.

in Fig. 26 are reflected here in the mean streamwise velocity contours. For case S10D [Fig. 28(b)], due to more turbulent entrainment of K from the top and bottom sides, the velocity deficit region (i.e., the region with blue contour color) is more round-shaped than those elliptical regions in cases HN10D [Fig. 28(a)] and HP10D [Fig. 28(c)]. Due to the stronger turbulent entrainment associated with $\langle \bar{u}'v' \rangle$ from the lateral direction, cases HN10D and HP10D also exhibit more wind speed recovery than case S10D. Between case HN10D and HP10D, the relatively strong vertical entrainment $\langle \bar{u}'w' \rangle$ around the upper shear layer in case HN10D [see Fig. 19(a)] causes more mean kinetic energy to be entrained from the high-speed free-stream wind above the VAWT rotor layer into the wake region, resulting in slightly more wind speed recovery than case HP10D. These differences in wind speed recovery rates can impact the wind power extraction for VAWTs in large arrays, which is further quantified and analyzed in Sec. IV E.

E. Power and structural bending moment

The power extracted by a VAWT can be calculated based on the wind-induced torque. Let $\theta_{n,m}$ be the instantaneous rotation azimuth angle of the n th element of the m th blade. Its contribution to the torque is

$$\tau_{n,m} = [F_{n,1}(\theta_{n,m}) \sin \theta_{n,m} - F_{n,2}(\theta_{n,m}) \cos \theta_{n,m}] R, \quad (12)$$

where the aerodynamic force components $F_{n,1}$ and $F_{n,2}$ are given in Appendix A by Eqs. (A1) and (A2), respectively. The instantaneous power extracted by the individual VAWT is

$$P = \sum_{m=1}^{N_b} \sum_{n=1}^{N_c} \tau_{n,m} \Omega, \quad (13)$$

and the corresponding power coefficient is

$$C_p = \frac{P}{0.5 \rho H D U_{10}^3}. \quad (14)$$

Here, U_{10} is the mean inflow wind speed from the precursor simulation measured at the 10 m height,¹⁹ which is estimated to be $U_{10} = 11.79$ m/s for the LES cases presented in this study.

Similar to the statistical analyses presented in Secs. IV B–IV D, here the mean power coefficients $\langle \bar{C}_p \rangle$ of different VAWT rows are calculated by time average as well as ensemble average among VAWTs in the same row. The values of $\langle \bar{C}_p \rangle$ for all nine simulation cases are shown in Fig. 29. VAWTs in the first row of each case can extract more power because they face the faster undisturbed wind, while individual VAWTs inside the array produce less power due to the wake effect from the upstream VAWTs. In each of the nine simulation cases, the mean power coefficient converges nearly to a constant value beyond $(x - x_1) / D \approx 20$, which corresponds to the fully developed

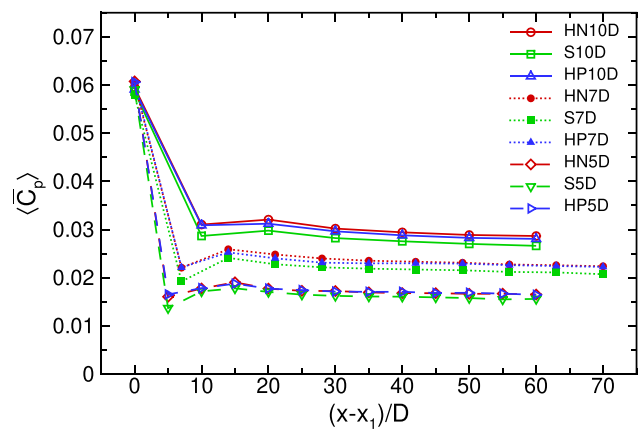


FIG. 29. Mean power coefficients $\langle \bar{C}_p \rangle$ for different VAWT rows in the nine cases.

flow region shown in Figs. 10–12. Reducing the streamwise turbine spacing S_x causes the local inflow wind speed to recover less, resulting in lower power coefficients for the VAWTs inside the array. Moreover, the VAWT blade geometry also causes noticeable effect on the power production. Taking as an example the $S_x = 10$ cases, the averaged power coefficients in the fully developed region of the array [denoted as $[C_p]_{fd}$ and calculated based on the VAWTs at $(x - x_1)/D > 21$] for the three different VAWT types follow the order of HN10D > HP10D > S10D, as shown in Table III. A similar trend is observed for the cases with $S_x = 7$. For $S_x = 5$, both helical-bladed VAWT cases (i.e., HN5D and HP5D) show higher $[C_p]_{fd}$ than the straight-bladed VAWT case (i.e., S5D), with the value of case HP5D slightly higher than that of case HN5D. Overall, the cases with helical-bladed VAWTs exhibit about 4.94–7.33% higher power than the corresponding cases with the straight-bladed VAWT.

When designing commercial wind farms, it is important to evaluate the power production rate per unit land area when the availability and cost of land are important factors to consider. Following Calaf *et al.*²⁶ (also see Yang *et al.*³²), the extracted power density by VAWTs in the fully developed region of the array is defined as

$$P_d^* = \frac{[P]_{fd}}{S_x S_y D^2 \rho U_{10}^3} = \frac{[C_p]_{fd}}{S_x S_y (2D/H)}, \quad (15)$$

where $[P]_{fd}$ is the averaged power of VAWTs within the fully developed region of the array. Note that the contributions from the entrance region of the array [i.e., the first few rows of VAWTs at $(x - x_1)/D \leq 21$] are excluded from the calculation of P_d^* . For large commercial wind farms with many rows of VAWTs, the major fraction of the total power production is due to the contribution from VAWTs in the fully developed region and scales as $\sim P_d^* (S_x S_y D^2 N_{fd})$, where N_{fd} are the total number of VAWTs in the fully developed region spaced evenly with $S_x D$ and $S_y D$ in the x - and y -directions, respectively.

The values of P_d^* for the nine cases considered in this study are listed in Table III. Changing the spacing from $(S_x, S_y) = (10, 10)$ to $(7, 5)$ (corresponding to about 186% increase for the number of VAWTs per unit land area) results in about 125% increase in P_d^* between the corresponding cases with the same VAWT type. Further reducing the spacing from $(S_x, S_y) = (7, 5)$ to $(5, 5)$ (corresponding to about 40% increase for the number of VAWTs per unit land area) results in only 2.39–4.33% increase in P_d^* for the three different VAWT types. Thus, it is apparent that the $(S_x, S_y) = (7, 5)$ spacing is more economical choice than the $(S_x, S_y) = (5, 5)$ spacing considering its lower cost (i.e., fewer VAWTs for lower cost on initial installation and long-term maintenance) for achieving comparable P_d^* . To

determine which spacing is more economical between $(S_x, S_y) = (10, 10)$ and $(7, 5)$, an optimization analysis based on the actual cost of land space, VAWTs, and long-term maintenance will need to be performed.^{31,75} Note that it is computationally expensive to use LES for optimization analysis. Alternatively, previous studies (see, e.g., Meyers and Meneveau⁷⁵ and Stevens³¹) used low-cost parameterizations of wind farm flows instead of LES to determine the optimal spacings and layouts of turbines for HAWT-based wind farms. A similar optimization analysis may be conducted for VAWT-based wind farms, which goes beyond the scope of the present work and will be considered in a future study.

Moreover, the instantaneous torque and power of a VAWT can have considerable temporal variations due to the effect of its own rotation (during which each blade experiences rapid change of aerodynamic forces depending on the rotation azimuth angle) as well as the effect of turbulence in its local inflow. Here, the temporal fluctuation of a VAWT's power coefficient is defined as $C'_p = C_p - \overline{C_p}$, and its root mean square value (i.e., the standard deviation) is denoted as σ_{cp} . The averaged values of σ_{cp} based on the VAWTs in the same row, i.e., $\langle \sigma_{cp} \rangle$, are calculated for all the nine simulation cases and the results are shown in Fig. 30. For the straight-bladed VAWT, each blade is located at a specific rotation angle θ with a difference of $\pm 120^\circ$ relative to the rotation angles of the other two blades. As the straight-bladed VAWT rotates, the instantaneous power oscillates as the three blades rotate through the full range of the azimuth angle. In contrast, each blade of the two helical VAWTs considered in this study covers a 127° range of θ , and the combination of three blades allows the full coverage of the entire rotation circle at any instantaneous time of the rotation, resulting in much less temporal fluctuation of the power. As shown in Fig. 30(a), for each VAWT array spacing, the straight-bladed VAWT case exhibits much higher $\langle \sigma_{cp} \rangle$ than the two corresponding helical-bladed VAWT cases. For the averaged value of $\langle \sigma_{cp} \rangle$ based on the VAWTs in the fully developed region of the array, the cases with helical-bladed VAWTs exhibit about 47.6–60.1% reduction compared with the corresponding cases with straight-bladed VAWTs.

For each VAWT type, Fig. 30 also shows that $\langle \sigma_{cp} \rangle$ reduces if the VAWT spacing is reduced. Such reduction could be due to the reduction of local inflow wind speed caused by smaller spacing. Note that the mean power coefficient $\langle \overline{C_p} \rangle$ also reduces with the reduced VAWT spacing due to the wind speed reduction. The ratio $\langle \sigma_{cp} \rangle / \langle \overline{C_p} \rangle$ quantifies the relative magnitude of the temporal fluctuation with respect to the mean. As shown in Fig. 30(b), the values of $\langle \sigma_{cp} \rangle / \langle \overline{C_p} \rangle$ for the straight-bladed VAWT for the three different spacings are very close to each other (around 1.1), confirming that the temporal oscillation of power coefficient for the straight-bladed VAWT cases is dominated by the effect of blade rotation as discussed above.

TABLE III. The averaged power coefficient per VAWT ($[C_p]_{fd}$) and the corresponding extracted power density coefficient (P_d^*) for VAWTs located in the fully developed region of the array. The relative increment of power coefficient is defined with respect to the straight-bladed VAWT case of the same array spacing.

Spacing Case	$(S_x, S_y) = (10, 10)$			$(S_x, S_y) = (7, 5)$			$(S_x, S_y) = (5, 5)$		
	HN10D	S10D	HP10D	HN7D	S7D	HP7D	HN5D	S5D	HP5D
$[C_p]_{fd} (10^{-2})$	2.92	2.73	2.86	2.31	2.15	2.28	1.69	1.60	1.70
$P_d^* (10^{-4})$	2.60	2.43	2.55	5.86	5.46	5.78	6.00	5.67	6.03
Relative increase	7.00%	...	4.94%	7.33%	...	5.86%	5.82%	...	6.35%

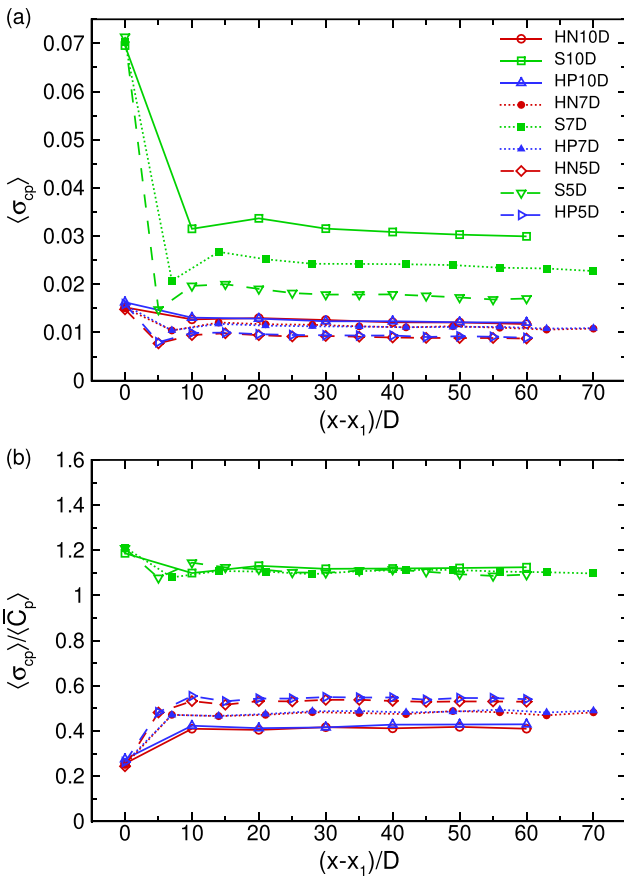


FIG. 30. Row-averaged standard deviation for the temporal variation of the power coefficient, $\langle \sigma_{cp} \rangle$, for different VAWT rows in the nine simulation cases. Panel (a) shows $\langle \sigma_{cp} \rangle$ and panel (b) shows $\langle \sigma_{cp} \rangle / \langle \bar{C}_p \rangle$.

In contrast, the cases associated with the two helical VAWTs exhibit similar dependence of $\langle \sigma_{cp} \rangle / \langle \bar{C}_p \rangle$ on the VAWT spacing. Due to the smooth coverage of θ by the three helical-shaped blades, the contribution to the temporal oscillation due to blade rotation is much less significant compared with the corresponding straight-bladed VAWT cases. This allows the effects of inflow turbulence to become more prominent. Note that all the helical-bladed VAWT cases have consistent free-stream inflow condition, resulting in very close values of $\langle \sigma_{cp} \rangle / \langle \bar{C}_p \rangle$ for the first VAWT row [Fig. 30(b)]. As the VAWT streamwise spacing is reduced, the turbulence intensity in the local inflow in front of each VAWT inside the array is increased [see Figs. 16(b) and 16(d)]. Consequently, the magnitudes of $\langle \sigma_{cp} \rangle / \langle \bar{C}_p \rangle$ in different helical-bladed VAWT cases follow the order of $\text{HN5D/HP5D} > \text{HN7D/HP7D} > \text{HN10D/HP10D}$ as shown in Fig. 30(b).

In addition to the effects on the wind power extraction, the VAWT blade geometry and the array spacing can also affect the wind load on the VAWT structure. Wind-induced oscillation can cause fatigue effect and impact the longevity of the VAWT system. Here, the spanwise bending moment relative to the root of the VAWT central axis is analyzed for demonstration purposes. The instantaneous spanwise bending moment M_y can be calculated based on

$$M_y = \sum_{m=1}^{N_b} \sum_{n=1}^{N_c} F_{n,1}(\theta_{n,m}) z_n, \quad (16)$$

where $F_{n,1}(\theta_{n,m})$ is the x -direction force component acting on the n th element of the m th blade, and z_n is the vertical coordinate of the blade element (assume the origin of the z coordinate is at the ground level and neglect the thickness of any bottom base structure). The dimensionless bending moment coefficient is defined as

$$C_y = \frac{M_y}{0.5\rho HD z_{eq} U_{10}^2}, \quad (17)$$

where HD corresponds to the projected area of the VAWT rotor and z_{eq} is the rotor equator height relative to the ground level (as defined in Sec. III).

For structure health, the crucial component of C_y is its temporal fluctuation part, which can cause fatigue effect to damage the VAWT structure. Here, the standard deviation for the temporal variation of C_y is denoted as σ_{C_y} and is calculated based on the LES data. The row-averaged values $\langle \sigma_{C_y} \rangle$ for different VAWT rows in the nine simulation cases are shown in Fig. 31. Similar to the blade effect on the power production, the straight-bladed VAWTs experience considerable temporal variations in C_y . Reducing the VAWT spacing causes the reduction of the local inflow speed (thus reducing the rotation speed) for VAWTs located inside the array, resulting in the reduction of $\langle \sigma_{C_y} \rangle$ for the straight-bladed VAWT as shown in Fig. 31. The twisted blades of the helical VAWTs help reduce the temporal variation of C_y by covering the full range of θ smoothly during the rotation. For the helical-bladed VAWTs, the cases with positive twist angle appear to have smaller $\langle \sigma_{C_y} \rangle$ than the corresponding negative twist angle cases. A close-up look of the flow field in the VAWT rotor region suggests that the difference in $\langle \sigma_{C_y} \rangle$ between the positive and negative helical-bladed VAWTs is caused by the effect of vertical flow generated by the twisted blade. Figure 32 shows the comparison between cases HN10D and HP10D for demonstration. In case HP10D, the helical blades induce additional upward flow motion in the rotor region relative to the straight-bladed VAWT case S10D [see around $(x - x_1)/D = 39.65$ in Fig. 32(d)], causing the distribution of the streamwise velocity fluctuation $\langle u'u' \rangle$ to be more biased toward the upper side of the rotor region

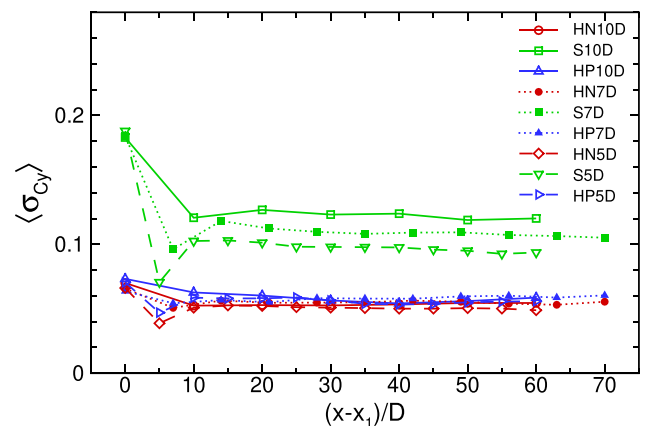


FIG. 31. Row-averaged standard deviation for the temporal variation of the spanwise bending moment, σ_{C_y} , for different VAWT rows in the nine simulation cases.

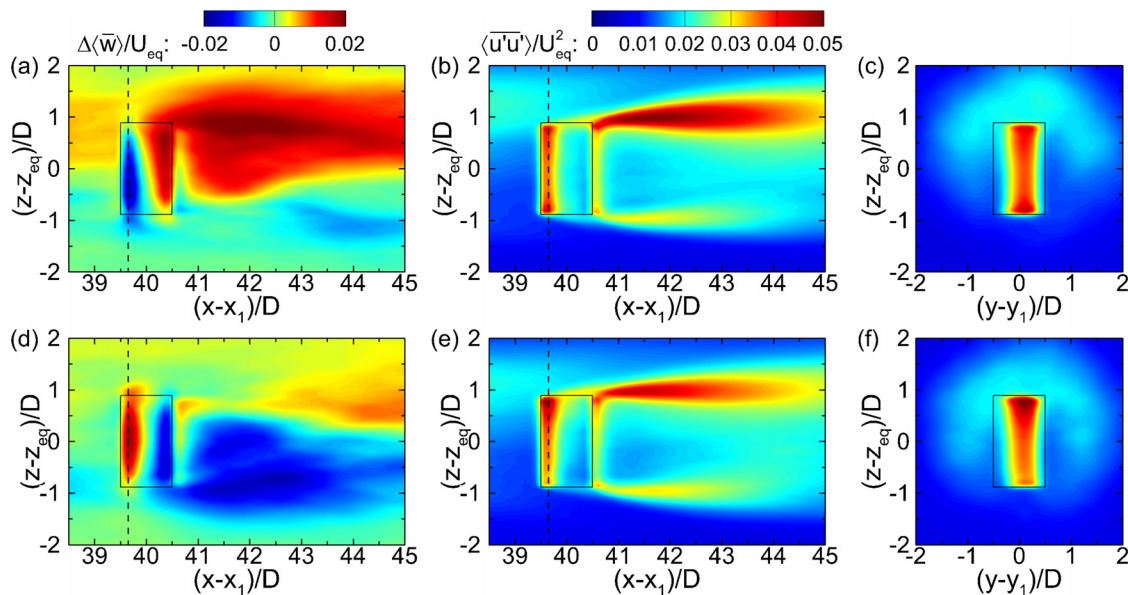


FIG. 32. Close-up views of the mean flow field near the fourth VAWT for cases HN10D (a)–(c) and HP10D (d)–(f). Panels (a) and (d) show $\Delta\langle\bar{w}\rangle$ and (b) and (e) show $\langle u'u' \rangle$ on the (x,z) -plane across the centerline of the VAWT column. Panels (c) and (f) show $\langle u'u' \rangle$ on the (y,z) -plane at $(x - x_1)/D = 39.65$ [indicated by the dashed line in (a) and (d)]. In each panel, the VAWT rotor location is indicated by the rectangle.

[Figs. 32(e) and 32(f)]. In contrast, the helical blades in case HN10D induces additional downward flow motion in the rotor region [Fig. 32(a)], which helps make $\langle u'u' \rangle$ more evenly distributed along the vertical direction. The bias of turbulent fluctuation inside the rotor region toward the upper side in case HP10D results in slightly higher $\langle \sigma_{C_p} \rangle$ than that in case HN10D.

V. DISCUSSION AND CONCLUSION

In this study, the turbulent flow characteristics in large arrays of VAWTs with finite streamwise length are investigated via LES modeling. A total of nine cases are simulated and analyzed, covering three different VAWT spacings [i.e., $(S_x, S_y) = (10, 10)$, (7.5) , and $(5, 5)$] and three different VAWT types (i.e., one straight-bladed VAWT and two helical-bladed VAWTs with opposite twist angles of $\gamma = \pm 127^\circ$). In each case, the array consists of a large number of VAWTs (i.e., 56, 176, and 208 for the three different spacings), which rotate independently based on the local inflow speed. The aerodynamic forces of each blade are modeled using ALM. The combination of LES and ALM allows the detailed wake flow characteristics inside the large array of VAWTs to be captured.

By performing systematic statistical analysis, the effects of VAWT blade geometry on the turbulent flow characteristics, VAWT power production, and structural bending moment fluctuation under different array spacing conditions are investigated. In all reported simulation cases, the flow characteristics in the VAWT array exhibit convergence toward a fully developed state after the VAWT row located around $(x - x_1)/D = 20$ toward the downstream direction. For the same array spacing, the two helical-bladed VAWTs are found to have about 4.94%–7.33% higher mean power production rate in the fully developed region than the corresponding straight-bladed VAWT cases. Statistical analyses of the flow field inside the VAWT array

indicate that the increased power for helical VAWTs is due to the enhanced lateral entrainment of mean kinetic energy to help recover the wake flow speed behind each VAWT. Compared with the straight-bladed VAWT, the helical-bladed VAWTs are found to also extract wind power much more smoothly, exhibiting about 47.6%–60.1% reduction in the temporal fluctuation of the power coefficient (estimated based on the averaged value of $\langle \sigma_{C_p} \rangle$ in the fully developed region of the array). The helical-bladed VAWTs also experience much less wind-induced oscillation in the spanwise bending moment relative to the base of the VAWT tower when compared with the straight-bladed VAWT, which suggests that using helical-bladed VAWTs may increase the longevity of the VAWT system and reduce the long-term maintenance cost.

It should be noted that due to the high computational cost for simulating large VAWTs arrays, the present study only includes a limited number of simulation cases that cover three different array spacings with all three VAWT types based on the same basic design (differing only in the blade twist angle). More simulations may need to be conducted in the future to consider additional VAWT designs, array spacings, array lengths, etc., in order to further generalize the understanding of the potential performance differences between helical-bladed and straight-bladed VAWTs.

It should also be noted that although the ALM-based LES model has been used as the high-fidelity model for uncertainty quantification of other lower-fidelity wind farm models,^{76,77} it may still produce uncertainties due to the complexity involved in modeling wind farm flows. Potential sources for uncertainties when using ALM-based LES to predict the performance of wind farms may include the wind direction variations due to large-scale weather system, LES grid resolution, SGS modeling, modeling or parameterization of the blade lift and drag, etc. Uncertainty quantification of LES model is quite challenging

and computationally expensive.⁷⁶ It goes beyond the scope of the current work but deserves further investigation in future studies.

ACKNOWLEDGMENTS

This research was supported by the National Science Foundation Fluid Dynamics Program under Grant No. 1804214 to D.Y. and Grant Nos. 1802476 and 2038071 to J.O.D. N.J.W. acknowledges support from the National Science Foundation Graduate Research Fellowship. M.G. and D.Y. acknowledge the use of the Sabine and Cary clusters from the Research Computing Data Core (RCDC) at the University of Houston. This work was authored, in part, by the National Renewable Energy Laboratory, operated by Alliance for Sustainable Energy, LLC, for the U.S. Department of Energy (DOE) under Contract No. DE-AC36-08GO28308. Funding provided by the U.S. Department of Energy Office of Energy Efficiency and Renewable Energy Wind Energy Technologies Office. The views expressed in the article do not necessarily represent the views of the DOE or the U.S. Government. The U.S. Government retains and the publisher, by accepting the article for publication, acknowledges that the U.S. Government retains a nonexclusive, paid-up, irrevocable, worldwide license to publish or reproduce the published form of this work, or allow others to do so, for U.S. Government purposes.

AUTHOR DECLARATIONS

Conflict of Interest

The authors have no conflicts to disclose.

Author Contributions

Masoumeh Gharaati: Conceptualization (equal); Data curation (lead); Formal analysis (lead); Investigation (lead); Methodology (lead); Visualization (lead); Writing – original draft (equal). **Nathaniel J. Wei:** Conceptualization (equal); Formal analysis (supporting); Investigation (supporting); Writing – review & editing (equal). **John O. Dabiri:** Conceptualization (equal); Formal analysis (supporting); Funding acquisition (equal); Investigation (supporting); Writing – review & editing (equal). **Luis A. Martinez-Tossas:** Investigation (supporting); Methodology (equal); Writing – review & editing (equal). **Di Yang:** Conceptualization (lead); Funding acquisition (equal); Investigation (equal); Methodology (equal); Project administration (lead); Writing – original draft (equal).

DATA AVAILABILITY

The data that support the findings of this study are available from the corresponding author upon reasonable request.

APPENDIX A: ACTUATOR LINE METHOD FOR MODELING VAWT FORCES

In this section, the implementation of ALM in the LES model is explained briefly. The important parameters for modeling the VAWT forces are denoted as following: R is the radius of the VAWT rotor (i.e., the radial distance from the central axis to the chord of each blade); $D = 2R$ is the diameter of the VAWT rotor; c is the chord length of the blade cross section; t_b is the cross-

sectional thickness of the blade; H is the vertical height of each blade; and Ω is the angular speed of the VAWT rotation. In this study, the VAWTs are set to rotate counterclockwise.

If each VAWT blade is discretized evenly into N_e elements, the vertical height of each blade element is $\Delta H = H/N_e$. For the n th blade element, the corresponding aerodynamic forces acting on it in the x - and y -directions as modeled as^{9,24,39,44,45,48}

$$F_{n,1} = -\frac{1}{2}\rho V_{rel}^2 c \Delta H [C_L^* \cos(\theta + \alpha) + C_D^* \sin(\theta + \alpha)], \quad (A1)$$

$$F_{n,2} = \frac{1}{2}\rho V_{rel}^2 c \Delta H [-C_L^* \sin(\theta + \alpha) + C_D^* \cos(\theta + \alpha)]. \quad (A2)$$

Here, θ is the azimuth angle of the blade rotation, $V_{rel} = \sqrt{(\tilde{u} - R \Omega \sin \theta)^2 + (\tilde{v} + R \Omega \cos \theta)^2}$ is the magnitude of the relative horizontal velocity of the local air inflow with respect to the blade element, and C_L^* and C_D^* are the lift and drag coefficients with dynamic stall correction.⁷⁸ The angle of attack of the blade element relative to the local inflow, α , can be determined based on the relative direction of the local wind inflow with respect to the local (s, n) coordinate system along the chord and radial directions of the turbine blade element as illustrated in Fig. 33. In the (s, n) coordinates, the local wind velocity vector is written as

$$\mathbf{V}_{local} = \tilde{V}_h \sin(\theta - \beta) \hat{\mathbf{e}}_s - \tilde{V}_h \cos(\theta - \beta) \hat{\mathbf{e}}_n, \quad (A3)$$

where $\hat{\mathbf{e}}_s$ is the unit vector along the blade element's chord direction, $\hat{\mathbf{e}}_n$ is the unit vector along the blade element's radial direction, $\tilde{V}_h = \sqrt{\tilde{u}^2 + \tilde{v}^2}$ is the magnitude of the inflow horizontal velocity, and $\beta = \arctan(\tilde{v}/\tilde{u})$ is the angle between the streamwise and spanwise inflow velocities. The relative horizontal velocity of the local air inflow with respect to the blade element in the (s, n) coordinates can be written as

$$\begin{aligned} \mathbf{V}_{rel} &= \mathbf{V}_{local} - R \Omega \hat{\mathbf{e}}_s \\ &= [\tilde{V}_h \sin(\theta - \beta) - R \Omega] \hat{\mathbf{e}}_s - \tilde{V}_h \cos(\theta - \beta) \hat{\mathbf{e}}_n. \end{aligned} \quad (A4)$$

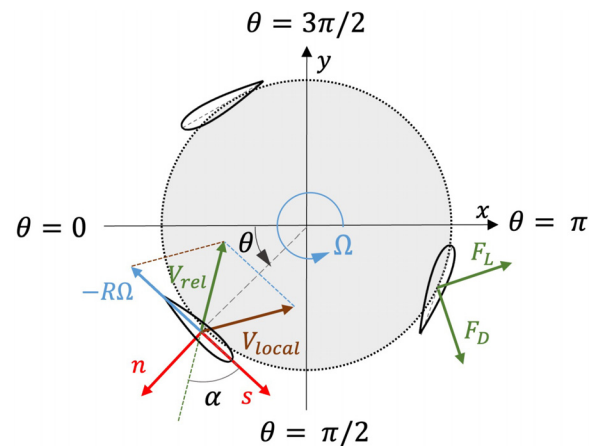


FIG. 33. Schematics of the (x, y) -plane view of the VAWT blades path and the physical quantities involved in the modeling of the aerodynamic forces.

TABLE IV. Simulation parameters and results for testing of domain height.

Case	VAWT type	Domain size (L_x, L_y, L_z) m	Grid resolution ($N_x \times N_y \times N_z$)	Blockage ratio	Array-averaged power coefficient
S10D	Straight-bladed	(165.6,144,20)	1058 × 920 × 300	1.6%	3.07×10^{-2}
S10D-32	Straight-bladed	(165.6,144,32)	1058 × 920 × 480	1%	3.14×10^{-2}
S5D	Straight-bladed	(165.6,144,20)	1058 × 920 × 300	3.2%	1.77×10^{-2}
S5D-32	Straight-bladed	(165.6,144,32)	1058 × 920 × 480	2%	1.76×10^{-2}

The corresponding angle of attack α is computed as

$$\alpha = \arctan\left(\frac{-\cos(\theta - \beta)}{-\sin(\theta - \beta) + R \Omega / \tilde{V}_h}\right). \quad (\text{A5})$$

In the present LES study, the modified Boeing–Vertol model⁷⁹ is adopted to model the effect of dynamic stall caused by the rapid changes in angle of attack during rotation.⁷⁸ With the dynamic stall correction, the effective angles of attack for lift and drag are modeled as⁷⁹

$$\alpha_L^* = \alpha - \gamma_L \zeta \sqrt{\left|\frac{c\dot{\alpha}}{2V_{\text{rel}}}\right|} \frac{\dot{\alpha}}{|\dot{\alpha}|}, \quad (\text{A6})$$

$$\alpha_D^* = \alpha - \gamma_D \zeta \sqrt{\left|\frac{c\dot{\alpha}}{2V_{\text{rel}}}\right|} \frac{\dot{\alpha}}{|\dot{\alpha}|}, \quad (\text{A7})$$

respectively, where $\dot{\alpha} = d\alpha/dt$ is the instantaneous rate of change of α , and the dimensionless model coefficients are given by

$$\gamma_L = 1.4 - 6\left(0.06 - \frac{t_b}{c}\right), \quad (\text{A8})$$

$$\gamma_D = 1 - 2.5\left(0.06 - \frac{t_b}{c}\right), \quad (\text{A9})$$

$$\zeta = 0.75 + 0.25 \frac{\dot{\alpha}}{|\dot{\alpha}|}. \quad (\text{A10})$$

The modified lift and drag coefficients after the dynamic stall correction are modeled as⁷⁹

$$C_L^* = \left(\frac{\alpha}{\alpha_L^* - \alpha_0}\right) C_L(\alpha_L^*), \quad (\text{A11})$$

$$C_D^* = C_D(\alpha_D^*), \quad (\text{A12})$$

where α_0 is the angle of zero lift (which is equal to 0° for symmetric airfoils), and C_L and C_D are the static lift and drag coefficients for the corresponding airfoil shape of the VAWT blade cross section, respectively. In the present LES study, the values for C_L and C_D are obtained from the empirical data reported in Sheldahl and Klimas.⁶⁴

In the LES model, a 3D Gaussian kernel method is used to smoothly distribute the forces computed by Eqs. (A1) and (A2) onto the computational grids around the blade element. The distributed body forces $f_{e,i}$ ($i = 1, 2$) for Eq. (2) are computed as³⁸

$$f_{e,i}(x, y, z) = \sum_{n=1}^{N_e} F_{n,i} G_n(x, y, z), \quad (\text{A13})$$

where $G_n(x, y, z) = \varepsilon^{-3} \pi^{-3/2} \exp(-r_n^2/\varepsilon^2)$ is the Gaussian kernel function, ε is the kernel width, and $r_n = \sqrt{(x - x_n)^2 + (y - y_n)^2 + (z - z_n)^2}$ is the distance between a space point (x, y, z) and the center point of the n th blade element (x_n, y_n, z_n) . The specific value for ε is given in Sec. III.

APPENDIX B: TEST OF SIMULATION DOMAIN HEIGHT

As reported by Sarlak *et al.*⁴³ based on LES tests, the domain height needs be adequate to ensure that the turbine blockage ratio does not exceed 5%. In Sarlak *et al.*,⁴³ the LES tests were done based on a HAWT in a wind tunnel, and the blockage ratio was defined as the ratio of the rotor swept area to the tunnel cross-sectional area. For the VAWTs array cases considered in this study, the blockage ratio may be defined as the VAWT rotor cross-sectional area to the domain cross-sectional area per VAWT (since there are multiple VAWTs per row of the array). In another LES study of infinite VAWT arrays, Hezaveh *et al.*¹⁷ used a simulation domain height that was 26.7 times of the VAWT rotor diameter D and 5.2 times of the VAWT rotor height H . For the array layouts considered in their study, the corresponding blockage ratio was reported to be below 3.75%. Two additional cases with increased domain height were tested in their study, and the reported array-averaged power coefficients showed an insignificant variation of about 2% (based on the values reported in Table II of Hezaveh *et al.*¹⁷).

The simulation domain height used in the present study is 20 m, which corresponds to $11.11D$ and $6.25H$. As listed in Table IV, the LES cases presented in this paper have the blockage ratios range from 1.6% for $(S_x, S_y) = (10, 10)$ to 3.2% for $(S_x, S_y) = (5, 5)$, which do not exceed the 5% threshold reported in Sarlak *et al.*⁴³ and is slightly lower than the upper bound reported in Hezaveh *et al.*¹⁷ Similar to Hezaveh *et al.*,¹⁷ two additional test cases S10D-32 and S5D-32 were performed (see Table IV), in which the domain heights were increased from 20 to 32 m and the corresponding blockage ratios were reduced to 1% and 2%, respectively. The LES tests show that the variation of the array-averaged power coefficient is 2.28% between cases S10D and S10D-32, and 0.56% between cases S5D and S5D-32. Therefore, the 20 m domain height is considered adequate and used in the rest of the simulation cases reported in the present study.

REFERENCES

1. Potrč, L., Čuček, M., Martin, and Z. Kravanja, “Sustainable renewable energy supply networks optimization—The gradual transition to a renewable energy system within the European Union by 2050,” *Renewable Sustainable Energy Rev.* **146**, 111186 (2021).

- ²Global Wind Energy Council, “Global Wind Report 2022,” Report (Global Wind Energy Council, 2022).
- ³J. F. Manwell, J. G. McGowan, and A. L. Rogers, *Wind Energy Explained*, 2nd ed. (Wiley, 2009).
- ⁴T. Burton, N. Jenkins, D. Sharpe, and E. Bossanyi, *Wind Energy Handbook* (Wiley, 2011).
- ⁵F. Porté-Agel, M. Bastankhah, and S. Shamsoddin, “Wind-turbine and wind-farm flows: A review,” *Boundary-Layer Meteorol.* **174**, 1–59 (2020).
- ⁶J. Contrell, T. Stehly, J. Johnson, J. O. Roberts, Z. Parker, G. Scott, and D. Heimiller, “Analysis of transportation and logistics challenges affecting the deployment of larger wind turbines: Summary of results,” Report No. NREL/TP-5000-61063 (National Renewable Energy Laboratory, 2014).
- ⁷M. Kinzel, Q. Mulligan, and J. O. Dabiri, “Energy exchange in an array of vertical-axis wind turbines,” *J. Turbul.* **13**, N38 (2012).
- ⁸M. Casini, “Small vertical axis wind turbines for energy efficiency of buildings,” *J. Clean Energy Technol.* **4**, 56–65 (2016).
- ⁹S. H. Hezaveh, E. Bou-Zeid, M. W. Lohry, and L. Martinelli, “Simulation and wake analysis of a single vertical axis wind turbine,” *Wind Energy* **20**, 713–730 (2017).
- ¹⁰L. Battisti, A. Brighenti, E. Benini, and M. R. Castelli, “Analysis of different blade architectures on small VAWT performance,” *J. Phys.: Conf. Ser.* **753**, 062009 (2016).
- ¹¹G. Brochier, P. Fraunie, C. Beguier, and I. Paraschivoiu, “Water channel experiments of dynamic stall on Darrieus wind turbine blades,” *J. Propul. Power* **2**, 445–449 (1986).
- ¹²P. Bachant and M. Wosnik, “Performance and near-wake measurements for a vertical axis turbine at moderate Reynolds number,” in Proceedings of the ASME Fluids Engineering Summer Meeting, 2013.
- ¹³D. B. Araya and J. O. Dabiri, “A comparison of wake measurements in motor-driven and flow-driven turbine experiments,” *Exp. Fluids* **56**, 150 (2015).
- ¹⁴M. Kinzel, D. B. Araya, and J. O. Dabiri, “Turbulence in vertical axis wind turbine canopies,” *Phys. Fluids* **27**, 115102 (2015).
- ¹⁵D. B. Araya and J. O. Dabiri, “Vertical axis wind turbine in a falling soap film,” *Phys. Fluids* **27**, 091108 (2016).
- ¹⁶D. B. Araya, T. Colonius, and J. O. Dabiri, “Transition to bluff-body dynamics in the wake of vertical-axis wind turbines,” *J. Fluid Mech.* **813**, 346–381 (2017).
- ¹⁷S. H. Hezaveh, E. Bou-Zeid, G. Cortina, L. Martinelli, J. Dabiri, and M. Kinzel, “Increasing the power production of vertical-axis wind-turbine farms using synergistic clustering,” *Boundary-Layer Meteorol.* **169**, 275–296 (2018).
- ¹⁸I. D. Brownstein, N. J. Wei, and J. O. Dabiri, “Aerodynamically interacting vertical-axis wind turbines: Performance enhancement and three-dimensional flow,” *Energies* **12**, 2724 (2019).
- ¹⁹N. J. Wei, I. D. Brownstein, J. L. Cardona, M. F. Howland, and J. O. Dabiri, “Near-wake structure of full-scale vertical-axis wind turbines,” *J. Fluid Mech.* **914**, A17 (2021).
- ²⁰A. Alaimo, A. Esposito, A. Messineo, C. Orlando, and D. Tumino, “3D CFD analysis of a vertical axis wind turbine,” *Energies* **8**, 3013–3033 (2015).
- ²¹M. Moghimi and H. Motawej, “Developed DMST model for performance analysis and parametric evaluation of Gorlov vertical axis wind turbines,” *Sustainable Energy Technol. Assess.* **37**, 100616 (2020).
- ²²Q. Cheng, X. Liu, H. S. Ji, K. C. Kim, and B. Yang, “Aerodynamic analysis of a helical vertical axis wind turbine,” *Energies* **10**, 575 (2017).
- ²³U. Divakaran, A. Ramesh, A. Mohammad, and R. K. Velamati, “Effect of helix angle on the performance of helical vertical axis wind turbine,” *Energies* **14**, 393 (2021).
- ²⁴M. Gharaati, S. Xiao, N. J. Wei, L. A. Martínez-Tossas, J. O. Dabiri, and D. Yang, “Large-eddy simulation of helical- and straight-bladed vertical-axis wind turbines in boundary layer turbulence,” *J. Renewable Sustainable Energy* **14**, 053301 (2022).
- ²⁵R. B. Cal, J. Lebrón, L. Castillo, H. S. Kang, and C. Meneveau, “Experimental study of the horizontally averaged flow structure in a model wind-turbine array boundary layer,” *J. Renewable Sustainable Energy* **2**, 013106 (2010).
- ²⁶M. Calaf, C. Meneveau, and J. Meyers, “Large eddy simulation study of fully developed wind-turbine array boundary layers,” *Phys. Fluids* **22**, 015110 (2010).
- ²⁷M. Calaf, M. B. Parlange, and C. Meneveau, “Large eddy simulation study of scalar transport in fully developed wind-turbine array boundary layers,” *Phys. Fluids* **23**, 126603 (2011).
- ²⁸X. Yang, S. Kang, and F. Sotiropoulos, “Computational study and modeling of turbine spacing effects in infinite aligned wind farms,” *Phys. Fluids* **24**, 115107 (2012).
- ²⁹R. J. Stevens, J. Graham, and C. Meneveau, “A concurrent precursor inflow method for Large Eddy Simulations and applications to finite length wind farms,” *Renewable Energy* **68**, 46–50 (2014).
- ³⁰R. J. Stevens and C. Meneveau, “Temporal structure of aggregate power fluctuations in large-eddy simulations of extended wind-farms,” *J. Renewable Sustainable Energy* **6**, 043102 (2014).
- ³¹R. J. Stevens, “Dependence of optimal wind turbine spacing on wind farm length,” *Wind Energy* **19**, 651–663 (2016).
- ³²D. Yang, C. Meneveau, and L. Shen, “Large-eddy simulation of offshore wind farm,” *Phys. Fluids* **26**, 025101 (2014).
- ³³D. Yang, C. Meneveau, and L. Shen, “Effect of downwind swells on offshore wind energy harvesting—A large-eddy simulation study,” *Renewable Energy* **70**, 11–23 (2014).
- ³⁴S. Xiao and D. Yang, “Large-eddy simulation-based study of effect of swell-induced pitch motion on wake-flow statistics and power extraction of offshore wind turbines,” *Energies* **12**, 1246 (2019).
- ³⁵J. O. Dabiri, “Potential order-of-magnitude enhancement of wind farm power density via counter-rotating vertical-axis wind turbine arrays,” *J. Renewable Sustainable Energy* **3**, 043104 (2011).
- ³⁶D. B. Araya, A. E. Craig, M. Kinzel, and J. O. Dabiri, “Low-order modeling of wind farm aerodynamics using leaky Rankine bodies,” *J. Renewable Sustainable Energy* **6**, 063118 (2014).
- ³⁷S. Xie, C. L. Archer, N. Ghaisas, and C. Meneveau, “Benefits of collocating vertical-axis and horizontal-axis wind turbines in large wind farms,” *Wind Energy* **20**, 45–62 (2017).
- ³⁸J. N. Sørensen and W. Z. Shen, “Numerical modeling of wind turbine wakes,” *J. Fluids Eng.* **124**, 393–399 (2002).
- ³⁹S. Shamsoddin and F. Porté-Agel, “Large eddy simulation of vertical axis wind turbine wakes,” *Energies* **7**, 890–912 (2014).
- ⁴⁰L. A. Martínez-Tossas, M. J. Churchfield, and S. Leonardi, “Large eddy simulations of the flow past wind turbines: Actuator line and disk modeling,” *Wind Energy* **18**, 1047–1060 (2015).
- ⁴¹L. A. Martínez-Tossas, M. J. Churchfield, and C. Meneveau, “A highly resolved large-eddy simulation of a wind turbine using an actuator line model with optimal body force projection,” *J. Phys.: Conf. Ser.* **753**, 082014 (2016).
- ⁴²L. A. Martínez Tossas, R. J. Stevens, and C. Meneveau, “Wind farm large-eddy simulations on very coarse grid resolutions using an actuator line model,” AIAA Paper No. 2016-1261, 2016.
- ⁴³H. Sarlak, T. Nishino, L. A. Martínez-Tossas, C. Meneveau, and J. N. Sørensen, “Assessment of blockage effects on the wake characteristics and power of wind turbines,” *Renewable Energy* **93**, 340–352 (2016).
- ⁴⁴S. Shamsoddin and F. Porté-Agel, “A large-eddy simulation study of vertical axis wind turbine wakes in the atmospheric boundary layer,” *Energies* **9**, 366 (2016).
- ⁴⁵M. Abkar and J. O. Dabiri, “Self-similarity and flow characteristics of vertical-axis wind turbine wakes: An LES study,” *J. Turbul.* **18**, 373–389 (2017).
- ⁴⁶M. J. Churchfield, S. Schreck, L. A. Martínez-Tossas, C. Meneveau, and P. R. Spalart, “An advanced actuator line method for wind energy applications and beyond,” AIAA Paper No. 2017-1998, 2017.
- ⁴⁷V. Mendoza and A. Goude, “Wake flow simulation of a vertical axis wind turbine under the influence of wind shear,” *J. Phys.: Conf. Ser.* **854**, 012031 (2017).
- ⁴⁸V. Mendoza, P. Bachant, C. Ferreira, and A. Goude, “Near-wake flow simulation of a vertical axis turbine using an actuator line model,” *Wind Energy* **22**, 171–188 (2019).
- ⁴⁹V. Mendoza, A. Chaudhari, and A. Goude, “Performance and wake comparison of horizontal and vertical axis wind turbines under varying surface roughness conditions,” *Wind Energy* **22**, 458–472 (2019).
- ⁵⁰See <https://lesgo.me.jhu.edu/> for “LES GO: A parallel pseudo-spectral large-eddy simulation code.”
- ⁵¹D. K. Lilly, “The representation of small-scale turbulence in numerical simulation experiments,” in Proceedings of the IBM Scientific Computing Symposium on Environmental Sciences, 1967.
- ⁵²J. Smagorinsky, “General circulation experiments with the primitive equations,” *Mon. Weather Rev.* **91**, 99–164 (1963).

- ⁵³E. Bou-Zeid, C. Meneveau, and M. Parlange, "A scale-dependent Lagrangian dynamic model for large eddy simulation of complex turbulent flows," *Phys. Fluids* **17**, 025105 (2005).
- ⁵⁴M. Germano, U. Piomelli, P. Moin, and W. H. Cabot, "A dynamic subgrid-scale eddy viscosity model," *Phys. Fluids A* **3**, 1760–1765 (1991).
- ⁵⁵F. Porté-Agel, C. Meneveau, and M. B. Parlange, "A scale-dependent dynamic model for large-eddy simulation: Application to a neutral atmospheric boundary layer," *J. Fluid Mech.* **415**, 261–284 (2000).
- ⁵⁶C. Meneveau and J. Katz, "Scale-invariance and turbulence models for large-eddy simulation," *Annu. Rev. Fluid Mech.* **32**, 1–32 (2000).
- ⁵⁷C. Meneveau, T. S. Lund, and W. H. Cabot, "A Lagrangian dynamic subgrid-scale model of turbulence," *J. Fluid Mech.* **319**, 353–385 (1996).
- ⁵⁸X. Yang and F. Sotiropoulos, "LES investigation of infinite staggered wind-turbine arrays," *J. Phys.: Conf. Ser.* **555**, 012109 (2014).
- ⁵⁹C.-H. Moeng, "A large-eddy-simulation model for the study of planetary boundary-layer turbulence," *J. Atmos. Sci.* **41**, 2052–2062 (1984).
- ⁶⁰J. Albertson and M. Parlange, "Surface length scales and shear stress: Implications for land-atmosphere interaction over complex terrain," *Water Resour. Res.* **35**, 2121–2132, <https://doi.org/10.1029/1999WR900094> (1999).
- ⁶¹F. k Chow, R. L. Street, M. Xue, and J. H. Ferziger, "Explicit filtering and reconstruction turbulence modeling for large-eddy simulation of neutral boundary layer flow," *J. Atmos. Sci.* **62**, 2058–2077 (2005).
- ⁶²O. Coceal, T. G. Thomas, L. P. Castro, and S. E. Belcher, "Mean flow and turbulence statistics over groups of urban-like cubical obstacles," *Boundary-Layer Meteorol.* **121**, 491–519 (2006).
- ⁶³J. D. Albertson, "Large eddy simulation of land-atmosphere interaction," Ph.D. thesis (University of California, Davis, 1996).
- ⁶⁴R. E. Sheldahl and P. C. Klimas, "Aerodynamic characteristics of seven symmetrical airfoil sections through 180-degree angle of attack for use in aerodynamic analysis of vertical axis wind turbines," Report No. SAND-80-2114 (Sandia National Labs, 1981).
- ⁶⁵P. R. Spalart, "Direct numerical study of leading-edge contamination," in *Fluid Dynamics of Three-Dimensional Turbulent Shear Flows and Transition*, 1988.
- ⁶⁶T. Colonius, "Modeling artificial boundary conditions for compressible flow," *Annu. Rev. Fluid Mech.* **36**, 315–345 (2004).
- ⁶⁷P. Schlatter, N. Adams, and L. Kleiser, "A windowing method for periodic inflow/outflow boundary treatment of non-periodic flows," *J. Comput. Phys.* **206**, 505–535 (2005).
- ⁶⁸S. Chester, C. Meneveau, and M. B. Parlange, "Modeling turbulent flow over fractal trees with renormalized numerical simulation," *J. Comput. Phys.* **225**, 427–448 (2007).
- ⁶⁹E. Bou-Zeid, C. Meneveau, and M. B. Parlange, "Large-eddy simulation of neutral atmospheric boundary layer flow over heterogeneous surfaces: Blending height and effective surface roughness," *Water Resour. Res.* **40**, W02505, <https://doi.org/10.1029/2003WR002475> (2004).
- ⁷⁰J. Kleissl, V. Kumar, C. Meneveau, and M. B. Parlange, "Numerical study of dynamic Smagorinsky models in large-eddy simulation of the atmospheric boundary layer: Validation in stable and unstable conditions," *Water Resour. Res.* **42**, W06D10, <https://doi.org/10.1029/2005WR004685> (2006).
- ⁷¹L. A. Martínez-Tossas, M. J. Churchfield, and C. Meneveau, "Optimal smoothing length scale for actuator line models of wind turbine blades based on Gaussian body force distribution," *Wind Energy* **20**, 1083–1096 (2017).
- ⁷²L. P. Chamorro and F. Porté-Agel, "Turbulent flow inside and above a wind farm: A wind-tunnel study," *Energies* **4**, 1916–1936 (2011).
- ⁷³S. P. Pope, *Turbulent Flows* (Cambridge University Press, 2000).
- ⁷⁴J. Meyers and C. Meneveau, "Flow visualization using momentum and energy transport tubes and applications to turbulent flow in wind farms," *J. Fluid Mech.* **715**, 335–358 (2013).
- ⁷⁵J. Meyers and C. Meneveau, "Optimal turbine spacing in fully developed wind farm boundary layers," *Wind Energy* **15**, 305–317 (2012).
- ⁷⁶D. C. Maniacil, A. L. Frankel, G. Geraci, M. L. Blaylock, and M. S. Eldred, "Multilevel uncertainty quantification of a wind turbine large eddy simulation model," in 7th European Conference on Computational Fluid Dynamics, 2018.
- ⁷⁷J. Zhang and X. Zhao, "Quantification of parameter uncertainty in wind farm wake modeling," *Energy* **196**, 117065 (2020).
- ⁷⁸W. J. McCroskey, "The phenomenon of dynamic stall," Report No. 81264 (NASA, 1981).
- ⁷⁹R. Gormont, "A mathematical model of unsteady aerodynamics and radial flow for application to helicopter rotors," Report No. 72-67 (Army Air Mobility Research and Development Laboratory, 1973).